Rapid O_3 assimilations – Part 1: background and local contributions to tropospheric O_3 changes in China in 2015-2020

Rui Zhu[1], Zhaojun Tang[1], Xiaokang Chen[1], Xiong Liu[2] and Zhe Jiang[1]*

[1]School of Earth and Space Sciences, University of Science and Technology of China, Hefei, Anhui, 230026, China.
[2]Center for Astrophysics | Harvard & Smithsonian, Cambridge, MA 02138, USA.

*Correspondence to: Zhe Jiang (zhejiang@ustc.edu.cn)

Abstract

A single ozone (O_3) tracer mode was developed in this work to build the capability of the GEOS-Chem model for rapid O_3 simulation. The single O_3 tracer simulation demonstrates consistency with the GEOS-Chem full chemistry simulation, with dramatic reductions in computational costs of approximately 91-94%. The single O_3 tracer simulation was combined with surface and Ozone Monitoring Instrument (OMI) O_3 observations to investigate the changes in tropospheric O_3 over eastern (E.) China in 2015-2020. The assimilated O_3 concentrations demonstrate good agreement with O_3 observations: surface O_3 concentrations are 43.2, 41.8 and 42.1 ppb, and tropospheric O_3 columns are 37.1, 37.9 and 38.0 DU in the simulations, assimilations and observations, respectively. The assimilations indicate rapid rises in surface O_3 concentrations by 1.60 (spring), 1.16 (summer), 1.47 (autumn) and 0.80 (winter) ppb yr^{-1} over E. China in 2015-2020, and the increasing trends are underestimated by the a priori simulations. More attention is suggested to the rapid increases in O_3 pollution in spring and autumn. We find stronger rises in tropospheric O_3 columns over highly polluted areas due to larger local contributions, for example, 0.12 DU yr^{-1} (North China Plain) in contrast to -0.29 (Sichuan Basin) -0.25 DU yr^{-1} (Southern China). Furthermore, our analysis demonstrated noticeable contributions of the interannual variability in background O_3 to the trends in surface O_3 (particularly in the summer) and tropospheric O_3 columns over E. China in 2015-2020. This work highlights the importance of rapid simulations and assimilations to extend and interpret

atmospheric O_3 observations.

1. Introduction

Tropospheric ozone (O_3) is produced when volatile organic compounds (VOCs) and carbon monoxide (CO) are photochemically oxidized in the presence of nitrogen oxides (NO_x). Tropospheric O_3 has important influences on the climate (Mickley, 2004; Iglesias-Suarez et al., 2018), atmospheric oxidation capacity (Thompson, 1992; Prinn, 2003), human health and crop growth (Zhang et al., 2021; Li et al., 2022). The important role of O_3 in the atmosphere has led to many efforts focusing on O_3 observations that have improved our understanding of atmospheric O_3 (Logan et al., 2012; Oetjen et al., 2016; Parrish et al., 2021). The limited spatial coverage of O_3 observations promotes the efforts of spatial extensions of O_3 observations (Chang et al., 2015; Peng et al., 2016). Recent advances in machine learning techniques further provide a new method to extend O_3 observations by fusing satellite and surface observations (Li et al., 2020; Liu et al., 2022; Wei et al., 2022).

Chemical transport models (CTMs), as powerful tools, have been widely used to simulate and interpret observed O_3 variabilities (Parrington et al., 2012; Jiang et al., 2016; Li, Ke et al., 2019). Despite the advances in CTMs, an accurate simulation of observed O_3 is still challenging because of uncertainties in physical and chemical processes (Peng et al., 2021; Chen et al., 2022), emission inventories (Elguindi et al., 2020; Jiang et al., 2022) and coarse model resolutions (Schaap et al., 2015; Benavides et al., 2021). Furthermore, the high computational cost is a bottleneck for rapid simulations, which poses a possible barrier to better understanding tropospheric O_3. Alternatively, researchers may consider simulations of atmospheric O_3 with the archived O_3 product and loss rates. For example, the tagged-O_x mode of the GEOS-Chem model has been used to analyze the sources and transport of tropospheric O_3 (Zhang et al., 2008; Zhu et al., 2017; Han et al., 2018). However, it may not be an ideal choice to perform O_3

57 simulations based on the tagged-O_x mode because O_x is the combination of multiple species,
58 including O_3, and thus cannot be accurately compared with O_3 observations.

59 In this study, we developed the single O_3 tracer mode (tagged-O_3) of the GEOS-Chem
60 model, driven by archived O_3 product and loss rates provided by GEOS-Chem full chemistry
61 simulations, to build the capability of the GEOS-Chem model for rapid simulations of
62 tropospheric O_3 (rather than O_x). Data assimilations, by combining modeled and observed O_3
63 concentrations, can take advantage of both simulations and observations to produce more
64 accurate O_3 concentrations (Parrington et al., 2008; Ma et al., 2019; Huijnen et al., 2020). The
65 single O_3 tracer simulations were thus further combined with the Ozone Monitoring Instrument
66 (OMI) and China Ministry of Ecology and Environment (MEE) monitoring network O_3
67 observations (in this paper) and United States (US) Air Quality System (AQS) and European
68 AirBase network O_3 observations (in the companion paper, Zhu et al. (2023)) via a sequential
69 Kalman Filter (KF) assimilation system (Tang et al., 2022; Han et al., 2022) to perform a
70 comparative analysis to investigate the changes in tropospheric O_3 in eastern (E.) China in
71 2015-2020 (in this paper) and the US and Europe in 2005-2020 (Zhu et al., 2023).

72 Satellite instruments provide globally covered O_3 observations that are sensitive to O_3
73 concentrations in the free troposphere. The OMI-based assimilations can thus reflect the
74 optimized adjustments in both global background and local O_3 concentrations. On the other
75 hand, surface observations are sensitive to local O_3 concentrations. Surface observation-based
76 assimilations can reflect the optimized adjustments in local contributions, and the information
77 of local contributions can be transported into the free troposphere via vertical convection in the
78 assimilation processes, which is different from the fusion of satellite and surface observations
79 (Li et al., 2020; Liu et al., 2022; Wei et al., 2022). Consequently, a comparative analysis by
80 assimilating satellite and surface O_3 observations is useful for better characterization of O_3
81 changes in the surface and free troposphere. Furthermore, the low computational costs of the

single O_3 tracer simulations allow us to design and perform different experiments much more efficiently. Multiple simulation and assimilation experiments (see details in Table 1) were thus conducted in this work to analyze the impacts of background O_3 (particularly, the interannual and seasonal variabilities in the background O_3 as well as optimization in the background O_3) and local O_3 formation on the changes in surface and free tropospheric O_3 over E. China.

This paper is organized as follows: in Section 2, we provide descriptions of the MEE and OMI O_3 observations, the GEOS-Chem model and the single O_3 tracer simulation and assimilation system used in this work. Tropospheric O_3 changes in E. China in 2015-2020 are then demonstrated in Section 3 by assimilating MEE and OMI O_3 observations. As shown in Fig. 1, five regions (i.e., North China Plain (#1), Yangtze River Delta (#2), Central China (#3), Sichuan Basin (#4) and Southern China (#5)) are defined within the E. China domain. Regions #1 and #2 are defined as highly polluted regions by excluding grids with low and medium anthropogenic NO_x emissions. Tropospheric O_3 changes over these regions are discussed to investigate the possible regional discrepancies in surface and free tropospheric O_3 associated with different local pollution levels. Our conclusions follow in Section 4.

2. Data and Methods

2.1 Surface O_3 measurements

We use MEE surface in situ O_3 concentration data (https://quotsoft.net/air/) for the period 2015-2020. These real-time monitoring stations report hourly concentrations of criteria pollutants from 1691 sites in 2020. All stations (1441 urban sites and 250 urban background sites) are assimilated in our analysis. Concentrations were reported by the MEE in $\mu g\ m^{-3}$ under standard temperature (273 K) until 31 August 2018. This reference state was changed on 1 September 2018 to 298 K. We converted the O_3 concentrations to ppb and rescaled the post-August 2018 concentrations to the standard temperature (273 K) to maintain consistency in the

trend analysis. It should be noted that the assimilation of O_3 observations from urban and urban background sites may result in possible overestimation of surface O_3 concentrations over rural areas.

2.2 OMI PROFOZ product

The OMI instrument was launched in July 2004 on the Aura spacecraft with a spatial resolution of 13 × 24 km (nadir view). It provides globally covered measurements with backscattered sunlight in the ultraviolet–visible range from 270 to 500 nm (UV1: 270–310 nm; UV2: 310–365 nm; visible: 350–500 nm). In this study, we use the OMI O_3 profile retrieval product (PROFOZ v0.9.3, level 2, Liu et al. (2010); Huang et al. (2017)) from the Smithsonian Astrophysical Observatory (SAO). The retrieval uses the vector linearized discrete ordinate radiative transfer model (VLIDORT) (Spurr, 2006) and Bayesian optimal estimation. Profiles of partial O_3 columns (unit: DU) are retrieved in the spectral region of 270–330 nm with 24 vertical layers: approximately 2.5 km for each layer from the surface to approximately 60 km. The following filters are applied in our analysis following Huang et al. (2017): 1) nearly clear-sky scenes with effective cloud fraction < 0.3; 2) solar zenith angles (SZA) < 75°; and 3) fitting root mean square (RMS, ratio of fitting residuals to assumed measurement error) < 2.0.

Starting in 2009, anomalies were found in the OMI data and diagnosed as attenuated measured radiances in certain cross-track positions. This instrument degradation has been referred to as the "row anomaly". To enhance the quality and stability of the data, only across-track positions between 4-11 (within 30 positions in the UV1 channels) are assimilated in our main assimilation experiment (Exp. #8). This treatment is similar to the production of row-isolated data by using across-track positions between 3-18 (within 60 positions in the UV2 channels) in the OMI/MLS O_3 data (Ziemke et al., 2019; Wang, X. et al., 2022). The effects of the usage of row-isolated data will be evaluated by comparing the main assimilation experiment with the sensitivity assimilation experiment (Exp. #10) by assimilating OMI O_3 observations

at across-track positions 4-27.

The modeled tropospheric O_3 profiles in the assimilation processes and subsequent analyses are convolved by using the OMI retrieval averaging kernels and a priori O_3 profile based on the following equation (Liu et al., 2010; Huang et al., 2017):

$$\hat{\boldsymbol{x}} = \boldsymbol{x}_{\mathrm{a}} + \mathbf{A}(\boldsymbol{x} - \boldsymbol{x}_{\mathrm{a}}) \qquad \text{(Eq. 1)}$$

where $\hat{\boldsymbol{x}}$ is the modeled O_3 profile convolved by the retrieval averaging kernels, $\boldsymbol{x}_a$ is the OMI a priori O_3 profile, $\boldsymbol{x}$ is the modeled O_3 profile, and $\mathbf{A}$ is the OMI averaging kernel matrix. Here $\mathrm{A(i,j)} = \frac{\partial \hat{x}_j}{\partial x_i}$, representing the sensitivity of the retrieved partial O_3 column (DU) at layer j to the change in O_3 (DU) at layer i. The unit for averaging kernels in this OMI product is DU/DU because the conversion from DU to ppb varies with altitude.

2.3 GEOS-Chem model configuration

The GEOS-Chem chemical transport model (http://www.geos-chem.org, version 12-8-1) is driven by assimilated meteorological data from MERRA-2. The GEOS-Chem full chemistry simulation includes fully coupled O_3-NO_x-VOC-halogen-aerosol chemistry. Our analysis is conducted at a horizontal resolution of nested 0.5°×0.625° over E. China with chemical boundary conditions archived every 3 hours from global simulations with 4°×5° resolution. Emissions are computed by the Harvard-NASA Emission Component (HEMCO). Global default anthropogenic emissions are from the CEDS (Community Emissions Data System) (Hoesly et al., 2018). Regional emissions are replaced by MEIC (Multiresolution Emission Inventory for China) in China and MIX in other regions of Asia (Li et al., 2017). The reference year for the CEDS inventory is 2010 with annual scaling factors in 2005-2014, and the reference year for the MEIC/MIX inventory is 2010 with annual scaling factors in 2008-2010 in the GEOS-Chem model. Open fire emissions are from the Global Fire Emissions Database (GFED4) (van der Werf et al., 2010).

Following Jiang et al. (2022), the total anthropogenic NO_x and VOC emissions in the GEOS-Chem model are scaled based on Zheng et al. (2018) and Li, M. et al. (2019) so that the modeled surface nitrogen dioxide (NO_2) and O_3 concentrations in the a priori simulations are identical to Jiang et al. (2022) in 2005-2018. The total anthropogenic NO_x and VOC emissions in 2019-2020 are further scaled based on linear projections. The total anthropogenic NO_x emissions in the a priori simulations declined by 19% in China in 2015-2020. The total anthropogenic VOC emissions in the a priori simulations increased by 1% in China in 2015-2020. We refer the reader to Jiang et al. (2022) for the details of the model configuration and performance, particularly the modeled trends of surface and tropospheric column NO_2 in 2005-2018.

2.4 Single O_3 tracer simulation

A new chemical mechanism was developed in this work to allow the running of the single O_3 tracer mode (tagged-O_3). As shown in Fig. S1 (see the SI), the package of the Kinetic PreProcessor (KPP) module was modified to define the production (PO_3) and loss (LO_3) of O_3. The GEOS-Chem full chemistry simulations with the updated KPP module were then performed to produce PO_3 and LO_3 every 20 minutes. Here the 20 minutes are selected to be the same as the chemical time step in the GEOS-Chem full chemistry mode to ensure consistency between the single O_3 tracer and full chemistry simulations. Finally, the single O_3 tracer simulation (tagged_o3_mod.F90) was performed by reading the archived PO_3 and LO_3 provided by the full chemistry simulations. Because we are interested in tropospheric chemistry, we archived O_3 concentrations instead of O_3 production and loss rates in the stratosphere in the full chemistry simulations. The archived stratospheric O_3 concentrations were read in the single O_3 tracer simulation process as boundary conditions to ensure a reasonable stratospheric-tropospheric O_3 exchange.

The major advantage of the single O_3 tracer simulation is dramatic reductions in

computational costs by approximately 91%-94%; for example, the computational costs (hours of wall time for one year simulation) are 57.5 and 5.2 hours at the global scale (4°×5°) and 80.2 and 4.5 hours within the nested China domain (0.5°×0.625°) by full chemistry and single O_3 tracer simulations, respectively. Consequently, once PO_3 and LO_3 are produced, the computational costs of performing additional single O_3 tracer simulations are almost negligible. The low computational costs of the single O_3 tracer simulation allow us to design and perform different simulation and assimilation experiments much more efficiently. As shown in Table 1, there are 10 different simulation and assimilation experiments performed in this work, which requires 4812 hours (wall time) with the full chemistry simulation but only 270 hours (wall time) with the single O_3 tracer simulation.

Here we evaluate the consistency in modeled O_3 concentrations between single O_3 tracer and full chemistry simulations. Fig. 2A1-A5 show the annual and seasonal averages of the surface maximum daily 8-hour average (MDA8) O_3 over E. China in 2015-2020 from the full chemistry simulation. The modeled surface MDA8 O_3 concentrations are as high as 60-70 ppb in the summer and as low as 10-20 ppb in the winter over northern China. The simulation with the single O_3 tracer mode (Fig. 2B1-B5) demonstrates spatial consistency with the full chemistry simulation (Fig. 2A1-A5) and temporal consistency at both the daily (Fig. 3A) and monthly (Fig. 3B) scales in 2015-2020. In contrast, the tagged-O_x mode of the GEOS-Chem model is driven by the archived production and loss of O_x, which is the combination of multiple species (O_x=O_3+NO_2+2NO_3+3N_2O_5+HNO_3+HNO_4+peroxyacylnitrates). There are large discrepancies between full chemistry (Fig. 2A1-A5) and tagged-O_x (Fig. 2C1-C5) simulations. As shown in Fig. 3, the O_x concentrations are higher than the O_3 concentrations by approximately 6 ppb, and the relative difference can reach 40% in the winter. Our analysis thus indicates the reliability of the single O_3 tracer simulations developed in this work.

2.5 Data assimilation method

We employ the sequential KF to assimilate O_3 observations, which has been used in recent studies to optimize tropospheric CO concentrations (Tang et al., 2022; Han et al., 2022). As a brief description of the assimilation algorithm, the forward model (**M**) predicts the O_3 concentration ($\boldsymbol{x}_{\mathrm{at}}$) at time t:

$$\boldsymbol{x}_{\mathrm{at}} = \mathbf{M}_t \boldsymbol{x}_{t-1} \quad \text{(Eq. 2)}$$

The optimized O_3 concentrations can be expressed as:

$$\boldsymbol{x}_t = \boldsymbol{x}_{\mathrm{at}} + \mathbf{G}_t(\boldsymbol{y}_t - \mathbf{K}_t \boldsymbol{x}_{\mathrm{at}}) \quad \text{(Eq. 3)}$$

where $\boldsymbol{y}_t$ is the observation and $\mathbf{K}_t$ represents the operation operator that projects O_3 concentrations from the model space to the observation space. $\mathbf{G}_t$ is the KF gain matrix, which can be described as:

$$\mathbf{G}_t = \mathbf{S}_{\mathrm{at}} \mathbf{K}_t^T (\mathbf{K}_t \mathbf{S}_{\mathrm{at}} \mathbf{K}_t^T + \mathbf{S}_\epsilon)^{-1} \quad \text{(Eq. 4)}$$

where $\mathbf{S}_{\mathrm{at}}$ and $\mathbf{S}_\epsilon$ are the model and observation covariances, respectively. The optimized O_3 concentrations provided by Eq. 3 are then forwarded (hourly) to Eq. 2. The model errors are assumed to be 50% because the objective of our assimilations is to provide dynamic extensions of atmospheric O_3 observations. The a posteriori O_3 concentrations with the assumption of 50% model errors are expected to match better with atmospheric O_3 observations. The measurement errors are calculated as $\varepsilon_0 = ermax + 0.0075 * \Pi_0$, where *ermax* is the base error (1.5 μg m^{-3}) and Π_0 represents the observed O_3 concentrations (unit: μg m^{-3}). The representation errors are calculated as $\varepsilon_r = \gamma \varepsilon_0 \sqrt{\Delta l / L}$, where γ is a scaling factor (0.5), Δl is the model resolution (~56 km in this study), and L represents the range that the observation can reflect, which depends on the station type (2 km for urban, 4 km for suburban). The total observation error is then defined as $\varepsilon_t = \sqrt{\varepsilon_0^2 + \varepsilon_r^2}$. Furthermore, the "superobservation" method was applied in this work to further reduce the influence of representative error (Miyazaki et al., 2017; Tang et al., 2022):

$$\omega_j = 1/\varepsilon_j^2 \quad \text{(Eq. 5)}$$

$$y_s = \sum_{j=1}^{k} \omega_j y_j / \sum_{j=1}^{k} \omega_j \qquad \text{(Eq. 6)}$$

$$1/\varepsilon_s^2 = \sum_{j=1}^{k} 1/\varepsilon_j^2 \qquad \text{(Eq. 7)}$$

where y_j is O_3 observation of the *j*th station, ω_j represents the weighting factor of the *j*th station, y_s and ε_s are the grid-based O_3 observations and errors (superobservation), respectively.

3. Results and Discussion

3.1 Surface O_3 by assimilating MEE O_3 observations

We first investigate the effects of surface O_3 observations on single O_3 tracer assimilations. O_3 at the surface level is formed by precursors mixed in the planetary boundary layer (PBL). Thus, it may not be accurate to assume that the differences between simulated and observed surface O_3 concentrations are completely caused by biased O_3 production and loss at the surface level. Here we adjust O_3 concentrations above the surface level within the PBL when assimilating surface O_3 observations:

$$\Delta O_3^n = \Delta O_3^1 \times \gamma^{n-1} \qquad \text{(Eq. 8)}$$

where ΔO_3^1 is the adjustment at the surface level calculated with Eq. 3; ΔO_3^n is the adjustment at model level *n*, which is based on ΔO_3^1 but decays exponentially with the increase in model level, and the decay speed is adjusted by the γ parameter. As shown in Table 1, three assimilation experiments (Exp. #5-#7) were conducted to evaluate the effects of the decay speed: 1) $\gamma = 0$ by assuming that the biased surface O_3 concentrations are completely caused by biased O_3 production and loss at the surface level; 2) $\gamma = 1$ by assuming full mixing of O_3 biases within the PBL; and 3) $\gamma = 0.8$ by assuming partial mixing of O_3 biases within the PBL, i.e., the adjustment at the 4th model level is approximately 50% of ΔO_3^1, and the adjustment at the 10th model level (close to the top of PBL) is approximately 10% of ΔO_3^1.

As shown in Fig. S2A (see the SI), the assimilated surface MDA8 O_3 concentrations show good agreement by using different γ parameters: 42.3, 41.8 and 42.0 ppb ($\gamma = 0$, 0.8 and 1.0) in 2015-2020; there are noticeable discrepancies in the trends of assimilated surface O_3 concentrations: 0.80, 1.24 and 1.50 ppb yr^{-1} ($\gamma = 0$, 0.8 and 1.0) in 2015-2020 (Fig. S2B), and the trends obtained by considering the mixing of O_3 biases ($\gamma = 0.8$ and 1.0) match better with MEE O_3 observations (1.77 ppb yr^{-1}). Fig. S3 (see the SI) further demonstrates tropospheric O_3 columns by assimilating MEE O_3 observations in 2015-2020. We find good agreement in the assimilated tropospheric O_3 columns by using different γ parameters, i.e., the mean tropospheric O_3 columns are 38.1, 37.9 and 37.9 DU, and the trends of tropospheric O_3 columns are 0.11, 0.17 and 0.21 ppb yr^{-1} ($\gamma = 0$, 0.8 and 1.0). Considering the better agreement in the trends of assimilated surface O_3 concentrations ($\gamma = 0.8$ and 1.0) with observations, we finally decide to set $\gamma = 0.8$ as our main assimilation setting by assuming partial mixing of O_3 biases within the PBL.

Fig. 4A1-A5 show the annual and seasonal averages of surface MDA8 O_3 observations from MEE stations in 2015-2020. Fig. 4C1-C5 show the annual and seasonal averages of the a posteriori O_3 concentrations by assimilating the MEE O_3 observations. As shown in Fig. 5, the assimilated O_3 concentrations (blue lines) show good agreement with MEE O_3 observations (red lines): the mean surface MDA8 O_3 in 2015-2020 are 43.2, 41.8 and 42.1 ppb (E. China), 42.4, 45.6 and 47.6 ppb (North China Plain), 44.6, 45.0 and 44.9 ppb (Yangtze River Delta), 45.1, 43.1 and 43.5 ppb (Central China), 45.7, 37.5 and 36.9 ppb (Sichuan Basin), and 43.2, 39.2 and 38.3 ppb (Southern China) in the a priori simulations, a posteriori simulations and MEE observations, respectively. It should be noted that Fig. 5A exhibits broadly good agreement between the a priori and a posteriori O_3 concentrations over E. China except for a larger difference in the summer. However, as shown in Fig. 4D1-D5, the good agreements between the a priori and a posteriori O_3 concentrations are caused by the counterbalance of

positive biases (i.e., overestimated surface O_3 in the a priori simulations over southern China) and negative biases (i.e., underestimated surface O_3 in the a priori simulations over northern China). The good agreements in Fig. 5A thus cannot represent good performance in the simulations of surface O_3 concentrations.

The assimilations exhibit noticeable declines in surface O_3 concentrations over regions #2-5 in June-July, and the declines are underestimated by the a priori simulations (Fig. 5C-F). The inaccurate simulation in June-July thus results in overestimated surface O_3 concentrations in the summer. There is dramatic seasonality in surface O_3 concentrations (Fig. 5): maximum in June in the North China Plain, May and August in the Yangtze River Delta, Central China and Sichuan Basin, and September-October in Southern China. Fig. 4E1-E5 exhibits the effects of seasonal variabilities in background O_3 (Exp. #3) by fixing background O_3 in the spring in the simulations. The fixed background O_3 has limited influences on surface O_3 concentrations, and consequently, the seasonality in surface O_3 concentrations is dominated by local contributions. As we expected, MDA8 O_3 concentrations are higher over areas with higher anthropogenic NO_x emissions, for example, 45.6 and 45.0 ppb in the North China Plain and Yangtze River Delta, respectively, in contrast to 43.1, 37.5 and 39.2 ppb in Central China, Sichuan Basin and Southern China. The influences of regional transport on surface O_3 concentrations are limited; for example, O_3 generated within the North China Plain PBL by setting O_3 formation rates within the North China Plain PBL to zero (Exp. #4) are mainly contained within the North China Plain (Fig. 4F1-F5).

3.2 Rapid increasing trends in surface O_3 concentrations

Here we investigate the changes in surface O_3 concentrations from observations and assimilations. As shown in Fig. 6B1-B5, the a priori simulation suggests slightly increasing trends of MDA8 O_3 in 2015-2020: 0.31 (spring), -0.12 (summer), 0.45 (autumn) and 0.40 (winter) ppb yr^{-1}, and the relative increasing trends are 0.7 (spring), -0.2 (summer), 1.1

(autumn) and 1.4 (winter) % yr^{-1}. The a priori simulation suggests increasing trends of surface O_3 concentrations in the summer over areas with higher local pollution levels, for example, 0.68 and 0.63 ppb yr^{-1} over the North China Plain and Yangtze River Delta, respectively, and decreasing trends of surface O_3 concentrations in the summer over areas with lower local pollution levels, for example, -0.83 and -1.01 ppb yr^{-1} over the Sichuan Basin and Southern China, respectively. The decreasing trends over areas with lower local pollution levels in the simulations are not surprising, given the decreases in anthropogenic NO_x emissions (Zheng et al., 2018; Jiang et al., 2022) and the reported NO_x-limited O_3 nonlinear chemical regimes in model simulations (Chen et al., 2021; Liu et al., 2021). Furthermore, as shown in Fig. 6D1-D5, the interannual variabilities in background O_3 (Exp. #2) are suggested to result in increases in surface O_3 concentrations in the a priori simulations in 2015-2020 by 0.02 (spring), 0.05 (summer), 0.02 (autumn) and 0.00 (winter) ppb yr^{-1}, and the relative contribution is particularly pronounced in the summer.

In contrast, the increasing trends in surface O_3 are much stronger in the assimilations. As shown in Table 2.1, our assimilation suggests 1.60 (spring), 1.16 (summer), 1.47 (autumn) and 0.80 (winter) ppb yr^{-1} increases in surface O_3 over E. China in 2015-2020, and the relative increasing trends are 3.4 (spring), 2.2 (summer), 3.7 (autumn) and 2.7 (winter) % yr^{-1}. The annual increasing trend (1.24 ppb yr^{-1}) in the assimilated surface O_3 concentrations is more consistent with the MEE O_3 observations (1.77 ppb yr^{-1}) which are comparable with the reported recent trends in surface O_3 concentrations in China of 1.25-2.0 ppb yr^{-1} (Mousavinezhad et al., 2021; Wei et al., 2022; Wang, W. et al., 2022). The increasing trends are weaker when the modeled surface O_3 concentrations are averaged over E. China (Table 2.2) instead of sampling at the locations and times of MEE observations: 0.71 (spring), 0.36 (summer), 0.69 (autumn) and 0.54 (winter) ppb yr^{-1} because most MEE stations are urban sites. Our analysis thus indicates a noticeable underestimation in the increasing trends of surface O_3

concentrations in China in the a priori simulations, particularly in the summer, despite the anthropogenic NO_x and VOC emissions having been scaled in the simulations following Jiang et al. (2022).

The changes in surface O_3 concentrations have significant regional and seasonal discrepancies. As shown in Tables S1-S5 (see the SI), our assimilations demonstrate strong increasing trends in surface O_3 concentrations in 2015-2020 in spring (1.94 ppb yr^{-1} or 3.8% yr^{-1}) and summer (2.52 ppb yr^{-1} or 4.0% yr^{-1}) over the North China Plain; in spring (2.21 ppb yr^{-1} or 4.4% yr^{-1}) and autumn (1.84 ppb yr^{-1} or 4.1% yr^{-1}) over the Yangtze River Delta; in spring (2.07 ppb yr^{-1} or 4.3% yr^{-1}) and autumn (2.09 ppb yr^{-1} or 4.7% yr^{-1}) over Central China; in spring (1.69 ppb yr^{-1} or 3.8% yr^{-1}) over the Sichuan Basin; and in autumn (2.21 ppb yr^{-1} or 4.9% yr^{-1}) over Southern China. While surface O_3 concentrations are higher over areas with higher anthropogenic NO_x emissions, the increasing trends in surface O_3 concentrations over Central China and Southern China are comparable with those in the North China Plain and Yangtze River Delta. Our analysis advises more attention to O_3 pollution in spring and autumn over areas with lower anthropogenic NO_x emissions because of the rapid increases in surface O_3 concentrations.

3.3 Tropospheric O_3 columns by assimilating OMI O_3 observations

Fig. 7A1-A5 show the annual and seasonal averages of tropospheric OMI O_3 columns in 2015-2020. OMI is sensitive to O_3 at different vertical levels (Huang et al., 2017; Fu et al., 2018), and thus, the standard KF algorithm (Eq. 3) was employed to adjust tropospheric O_3 vertical profiles with the application of OMI O_3 averaging kernels. Fig. 7C1-C5 show the annual and seasonal averages of the a posteriori tropospheric O_3 columns by assimilating OMI O_3 observations. The assimilated tropospheric O_3 columns show good agreement with OMI O_3 observations: the mean tropospheric O_3 columns in 2015-2020 (Table 2.3) are 37.1 DU in the a priori simulations and 37.9 and 38.0 DU in the a posteriori simulation and OMI observations,

355 respectively. The discrepancies between the a priori and a posteriori simulations in tropospheric
356 O_3 columns (Fig. 7) are smaller than those in surface O_3 concentrations (Fig. 4). A better
357 simulation capability in tropospheric column O_3 is expected because model simulation with
358 0.5°×0.625° horizontal resolution may not be enough to accurately resolve O_3 nonlinear
359 chemical regimes over urban surface stations.

360 The above assimilated tropospheric O_3 columns (Exp. #8) are driven by optimized O_3
361 background conditions provided by global assimilations of OMI O_3 as well as row-isolated
362 OMI data by using across-track positions between 4-11. Fig. 7E1-E5 exhibits the effects of
363 optimization on regional O_3 background conditions. The mean assimilated tropospheric O_3
364 column driven by the original O_3 background conditions is 37.6 DU (Exp. #9), which is slightly
365 lower than the 37.9 DU in the main assimilation (Exp. #8). The usage of original O_3 background
366 conditions can result in overestimations over southern China in the spring and winter, and
367 underestimations over northern China in the spring and summer (Fig. 7E1-E5). Fig. 7F1-F5
368 further exhibits the effects of the usage of row-isolated data. The mean assimilated tropospheric
369 O_3 column by assimilating OMI O_3 observations at across-track positions 4-27 is 37.7 DU (Exp.
370 #10), which is slightly lower than the 37.9 DU in the main assimilation (Exp. #8). The
371 underestimations in the assimilated tropospheric O_3 columns are particularly significant in the
372 spring and summer (Fig. 7F2-F3).

373 As shown in Fig. 8, the trends of tropospheric O_3 columns in 2015-2020 (Table 2.3) are
374 0.02 DU yr^{-1} in the a priori simulations and -0.17 and -0.30 DU yr^{-1} in the a posteriori
375 simulation and OMI observations, respectively. In contrast to the wide distributions of
376 increasing trends of O_3 at the surface level (Fig. 6), both OMI O_3 observations (-0.30 DU yr^{-1})
377 and the OMI-based assimilations (-0.17 DU yr^{-1}) suggest decreasing trends in tropospheric O_3
378 columns over E. Asia in 2015-2020 (Fig. 8). The decreasing trends are stronger in the summer
379 and weaker in the spring. Furthermore, the usage of original O_3 background conditions can

result in overestimated trend by approximately 0.08 DU yr^{-1} (Fig. 8D1); and the assimilation of OMI O_3 observations at across-track positions 4-27 can result in a similar overestimated trend, by approximately 0.08 DU yr^{-1} (Fig. 8E1). These discrepancies demonstrate the importance of optimized usages of regional O_3 background conditions and OMI O_3 observations in the assimilations.

3.4 Changes in tropospheric O_3 columns

The trends shown in Fig. 8 may not represent the actual tropospheric O_3 changes well because the convolution of OMI O_3 averaging kernels on the output O_3 profiles can affect the weights of the derived tropospheric columns to O_3 at different vertical levels. Consequently, Fig. 9 shows the annual and seasonal averages of tropospheric O_3 columns in which the output O_3 profiles are not convolved with OMI retrieval averaging kernels so that they can better represent the actual atmospheric O_3 state. The assimilated tropospheric O_3 columns are 37.9 and 38.8 DU (E. China), 42.9 and 43.7 DU (North China Plain), 47.5 and 48.1 DU (Yangtze River Delta), 47.4 and 48.1 DU (Central China), 43.8 and 44.6 DU (Sichuan Basin), and 39.6 and 40.6 DU (Southern China) in 2015-2020 by assimilating MEE and OMI O_3 observations, respectively.

In contrast to the higher surface MDA8 O_3 concentrations over areas with higher anthropogenic NO_x emissions, tropospheric O_3 columns over Central China and the Sichuan Basin are even higher than those over the highly polluted North China Plain. In addition, tropospheric O_3 columns obtained by assimilating MEE surface O_3 observations are lower than those obtained by assimilating OMI O_3 observations, and their difference is larger in the summer and smaller in the winter. As shown in Fig. S4 (see the SI), the impacts of different surface and satellite O_3 observations on the assimilated O_3 vertical profiles are limited. The assimilation of MEE surface O_3 observations leads to decreases in O_3 concentrations in the lower troposphere from the surface to 600 hPa levels over the Sichuan Basin and Southern

China; the assimilation of OMI O_3 observations leads to enhancement in O_3 concentrations in the middle and upper troposphere over the highly polluted North China Plain.

The assimilated tropospheric O_3 columns are maximum in June-July over the highly polluted North China Plain and March-May over other lower polluted regions (Fig. S5, see the SI). Fig. 9E1-E5 exhibit the effects of seasonal variabilities in background O_3 (Exp. #3). The fixed background O_3 in the spring can result in dramatic increases in tropospheric O_3 columns by 14.3 (summer), 15.1 (autumn) and 4.8 (winter) DU over E. China. Fig. 9F1-F5 further exhibit the effects of O_3 formation within the North China Plain PBL (Exp. #4) on tropospheric O_3 columns, which are 5.4 (spring), 8.1 (summer), 3.6 (autumn) and 1.3 (winter) DU over the North China Plain. In addition, as shown in Fig. S6 (see the SI), there is a larger enhancement in O_3 production rates in the free troposphere (600-300 hPa) over the North China Plain in the summer than in other lower polluted regions. Consequently, the spring maximum in tropospheric O_3 columns over lower polluted regions is caused by the enhanced background O_3 (Fig. 9E1-E5), and the summer maximum in tropospheric O_3 columns over the highly polluted North China Plain is caused by the local contributions from enhanced O_3 formation within the North China Plain PBL (Fig. 9F1-F5) and free troposphere (Fig. S6).

As shown in Fig. 10A1-A5, the trends of tropospheric O_3 columns in the a priori simulations in 2015-2020 are -0.02 (spring), 0.02 (summer), 0.29 (autumn) and 0.09 (winter) DU yr^{-1} over E. China. The interannual variability in background O_3 (Fig. 10D1-D5, Exp. #2) is suggested to have important contributions to the trends of tropospheric O_3 columns by 0.09 (spring), -0.11 (summer), -0.10 (autumn) and -0.08 (winter) DU yr^{-1}. The trends of assimilated tropospheric O_3 columns are 0.17 and -0.10 DU yr^{-1} (E. China), which are comparable with the reported recent trend in free tropospheric O_3 concentrations over China by -0.14 DU yr^{-1} (Dufour et al., 2021), and are 0.47 and 0.12 DU yr^{-1} (North China Plain), 0.45 and 0.13 DU yr^{-1} (Yangtze River Delta), 0.32 and -0.06 DU yr^{-1} (Central China), 0.03 and -0.29 DU yr^{-1}

(Sichuan Basin), and 0.06 and -0.25 DU yr^{-1} (Southern China) by assimilating MEE and OMI O_3 observations, respectively.

The stronger increasing trends in tropospheric O_3 columns over the highly polluted North China Plain (Fig. 10A1) are suggested to be caused by larger local contributions because of relatively uniform influences from interannual variability in background O_3 (Fig. 10D1). Higher positive trends by assimilating MEE observations are expected, given the increasing trends in surface O_3 concentrations (1.77 ppb yr^{-1}) and decreasing trends in OMI O_3 concentrations (-0.30 DU yr^{-1}) over E. China. Furthermore, it should be noted that while the Yangtze River Delta is defined as a highly polluted region in our analysis, its area is much smaller than that of the North China Plain (Fig. 1); thus, the impact of local contributions on tropospheric O_3 columns over the Yangtze River Delta is not as strong as that over the North China Plain.

4. Conclusion

A single O_3 tracer (tagged-O_3) mode was developed in this work to build the capability of the GEOS-Chem model for rapid simulations of tropospheric O_3. The single O_3 tracer simulation demonstrates consistency with the GEOS-Chem full chemistry simulation. In contrast, the O_x concentrations provided by the tagged-O_x mode are higher than the O_3 concentrations by approximately 6 ppb, and the relative difference can reach 40% in the winter. The computational costs of the single O_3 tracer mode are reduced by approximately 91-94% with respect to the full chemistry mode. For example, the computational costs (hours of wall time per simulation year) are 57.5 and 5.2 hours at the global scale (4°×5°) and 80.2 and 4.5 hours within the nested China domain (0.5°×0.625°) by full chemistry and single O_3 tracer simulations, respectively. The low computational costs allow us to design and perform different experiments much more efficiently. As shown in Table 1, 10 different simulation and assimilation experiments are performed in this work to analyze the impacts of background and

local contributions to surface and free tropospheric O_3 changes over E. China in 2015-2020, which requires 4812 hours (wall time) with the full chemistry simulation but only 270 hours (wall time) with the single O_3 tracer simulation.

The assimilated surface O_3 concentrations demonstrate good agreement with surface O_3 observations: 43.2, 41.8 and 42.1 ppb over E. China in a priori and a posteriori simulations and observations, respectively. We find noticeable biases in modeled surface O_3 concentrations, for example, overestimated surface O_3 over southern China and underestimated surface O_3 over northern China. The assimilations indicate rapidly increasing trends in surface O_3 concentrations by 1.60 (spring), 1.16 (summer), 1.47 (autumn) and 0.80 (winter) ppb yr^{-1} over E. China in 2015-2020, and the increasing trends are underestimated by the a priori simulations. While surface O_3 concentrations are higher over areas with higher anthropogenic NO_x emissions, the increasing trends in surface O_3 concentrations over Central China and Southern China are comparable with those in the North China Plain and Yangtze River Delta. Our analysis thus advises more attention to O_3 pollution in spring and autumn over areas with lower anthropogenic NO_x emissions because of the rapid increases in surface O_3 concentrations. The seasonality in surface O_3 concentrations is dominated by local contributions; however, the interannual variabilities in background O_3 have noticeable contributions to the increasing trends in surface O_3 particularly in the summer in the a priori simulations.

The assimilated tropospheric O_3 columns demonstrate good agreement with OMI observations: 37.1, 37.9 and 38.0 DU over E. China in a priori and a posteriori simulations (convolved with OMI retrieval averaging kernels) and OMI observations, respectively. The trends of assimilated tropospheric O_3 columns in 2015-2020 over E. China are 0.09 and -0.17 (spring), 0.17 and -0.22 (summer), 0.38 and 0.04 (autumn), and 0.12 and -0.02 (winter) by assimilating MEE and OMI O_3 observations, respectively. The large discrepancy by assimilating surface and satellite observations indicates the possible uncertainties in the derived

free tropospheric O_3 changes. The usage of optimized O_3 background conditions and row-isolated OMI data is important to produce more reliable results, for example, the usage of original O_3 background conditions can result in an overestimated trend by approximately 0.08 DU yr^{-1} in 2015-2020.

We find stronger increasing trends in tropospheric O_3 columns over highly polluted areas due to the larger local contributions, for example, 0.47 and 0.12 DU yr^{-1} (North China Plain) in contrast to 0.03 and -0.29 DU yr^{-1} (Sichuan Basin) and 0.06 and -0.25 DU yr^{-1} (Southern China) by assimilating MEE and OMI O_3 observations, respectively. The spring maximum in tropospheric O_3 columns over lower polluted regions is caused by the enhanced background O_3, and the summer maximum in tropospheric O_3 columns over the highly polluted North China Plain is caused by enhanced local O_3 formation. The interannual variabilities in background O_3 have important contributions to the trends in tropospheric O_3 columns; for example, the trends of tropospheric O_3 columns in 2015-2020 are -0.02 (spring), 0.02 (summer), 0.29 (autumn) and 0.09 (winter) DU yr^{-1} over E. China, and the contributions from interannual variability in background O_3 are 0.09 (spring), -0.11 (summer), -0.10 (autumn) and -0.08 (winter) DU yr^{-1} in the a priori simulations. Assimilations of both surface and satellite observations, as shown in this work, can provide useful information to better describe the changes in surface and free tropospheric O_3.

Code and data availability: The MEE O_3 data can be downloaded from https://quotsoft.net/air/. The AQS and AirBase surface O_3 data can be downloaded from https://www.eea.europa.eu/data-and-maps/data/aqereporting-8 and https://aqs.epa.gov/aqsweb/airdata/download_files.html#Row. The OMI PROFOZ product can be acquired at https://avdc.gsfc.nasa.gov/pub/data/satellite/Aura/OMI/V03/L2/OMPROFOZ/. The GEOS-

Chem model (version 12.8.1) can be downloaded from http://wiki.seas.harvard.edu/geos-chem/index.php/GEOS-Chem_12#12.8.1. The KPP module for tagged-O_3 simulations can be downloaded from https://doi.org/10.5281/zenodo.7545944.

Author Contributions: Z.J. designed the research. R.Z. developed the model code and performed the research. Z.J. and R.Z. wrote the manuscript. X.L. provided instruction for the usage of OMI data. All authors contributed to discussions and editing the manuscript.

Competing interests: The contact author has declared that neither they nor their co-authors have any competing interests.

Acknowledgments: We thank the China Ministry of Ecology and Environment (MEE), the United States Environmental Protection Agency and the European Environmental Agency for providing the surface O_3 measurements. The numerical calculations in this paper have been done on the supercomputing system in the Supercomputing Center of University of Science and Technology of China. This work was supported by the Hundred Talents Program of Chinese Academy of Science and National Natural Science Foundation of China (42277082, 41721002).

Table and Figures

Table 1. Single O_3 tracer simulation and assimilation experiments (Exp.) conducted in this work. Exp. #1: the main a priori simulation; Exp. #2: O_3 boundary conditions and stratospheric O_3 concentrations are fixed in 2015; Exp. #3: O_3 boundary conditions and stratospheric O_3 concentrations are fixed in the spring; Exp. #4: O_3 formation rates within the North China Plain PBL are set to zero; Exp. #5: the main assimilation by assimilating MEE surface O_3 observations with $\gamma = 0.8$; Exp. #6: only surface O_3 concentrations are adjusted ($\gamma = 0$); Exp. #7: full mixing of O_3 biases within the PBL ($\gamma = 1.0$); Exp. #8: the main assimilation by

assimilating OMI O_3 observations; Exp. #9: O_3 boundary conditions are not optimized; Exp. #10: assimilating OMI O_3 observations at across-track positions 4-27.

Table 2. Averages (with units ppb or DU) and trends (with units ppb yr^{-1} or DU yr^{-1}) of surface and tropospheric column O_3 concentrations in 2015-2020 over E. China from observations (MEE and OMI) and a priori (Exp. #1) and a posteriori (KF) simulations (Exp. #5 and #8). T2.1): the modeled surface O_3 is sampled at the locations and times of MEE surface O_3 observations; T2.2): the modeled surface O_3 is averaged over E. China (land only); T2.3): the output O_3 profiles from the a priori and a posteriori simulations are convolved with OMI O_3 averaging kernels; T2.4): the output O_3 profiles are NOT convolved with OMI O_3 averaging kernels. The uncertainties in the averages are calculated using the bootstrapping method. The trends and uncertainties in the trends are calculated using the linear fitting of averages by using the least squares method (see details in the SI).

Fig. 1. (A) Anthropogenic NO_x emissions over E. China in 2015; (B) Region definitions for the North China Plain (#1), Yangtze River Delta (#2), Central China (#3), Sichuan Basin (#4) and Southern China (#5). The different colors (red, gray and green) represent grids with high (highest 15%), medium (15-50%) and low (lowest 50%) anthropogenic NO_x emissions. Regions #1 and #2 are defined as highly polluted (HP) regions by excluding grids with low and medium anthropogenic NO_x emissions.

Fig. 2. Surface MDA8 O_3 in 2015-2020 (annual and seasonal averages) simulated by GEOS-Chem model with (A1-A5) full chemistry mode; (B1-B5) single O_3 tracer (tagged-O_3) mode; and (C1-C5) tagged-O_x mode. The 8-hour range of surface O_x is selected according to the time range of MDA8 O_3.

Fig. 3. (A) Daily averages of surface MDA8 O_3 over E. China in 2015-2020 from GEOS-Chem full chemistry (black), single O_3 tracer (tagged-O_3) (blue) and tagged-O_x (red) simulations; (B) Monthly averages of MDA8 O_3. The dashed lines in panel B are annual averages.

Fig. 4. Surface MDA8 O_3 in 2015-2020 (annual and seasonal averages) from (A1-A5) MEE stations; (B1-B5) GEOS-Chem a priori simulation (Exp. #1); (C1-C5) GEOS-Chem a posteriori simulation by assimilating MEE O_3 observations (Exp. #5); (D1-D5) Bias in the a priori simulations (Exp. #1 minus #5). (E1-E5) Effects of seasonal variabilities in background

O_3 (Exp. #3 minus #1); (F1-F5) Effects of O_3 formation within the North China Plain PBL (Exp. #4 minus #1).

Fig. 5. (A-F) Daily averages of surface MDA8 O_3 in 2015-2020 from MEE stations (red) and GEOS-Chem a priori (black, Exp. #1) and a posteriori (blue, Exp. #5) simulations by assimilating MEE O_3 observations. (G-L) Monthly averages of MDA8 O_3. The dashed lines in panels G-L are annual averages.

Fig. 6. Trends of surface MDA8 O_3 in 2015-2020 (annual and seasonal averages) from (A1-A5) MEE stations; (B1-B5) GEOS-Chem a priori simulation (Exp. #1); (C1-C5) GEOS-Chem a posteriori simulation by assimilating MEE O_3 observations (Exp. #5). (D1-D5) Effects of interannual variabilities in background O_3 (Exp. #1 minus #2).

Fig. 7. Tropospheric O_3 columns in 2015-2020 (annual and seasonal averages) from (A1-A5) OMI observations; (B1-B5) GEOS-Chem a priori simulation (Exp. #1); (C1-C5) GEOS-Chem a posteriori simulation by assimilating OMI O_3 observations (Exp. #8). (D1-D5) Bias in the a priori simulations (Exp. #1 minus #8). (E1-E5) Effects of optimization on regional O_3 background conditions (Exp. #9 minus #8); (F1-F5) Effects of the usage of row-isolated data (Exp. #10 minus #8). The output O_3 profiles are convolved with OMI averaging kernels.

Fig. 8. Trends of tropospheric O_3 columns in 2015-2020 (annual and seasonal averages) from (A1-A5) OMI observations; (B1-B5) GEOS-Chem a priori simulation (Exp. #1); (C1-C5) GEOS-Chem a posteriori simulation by assimilating OMI O_3 observations (Exp. #8). (D1-D5) Effects of optimization on regional O_3 background conditions (Exp. #9 minus #8); (E1-E5) Effects of the usage of row-isolated data (Exp. #10 minus #8). The output O_3 profiles are convolved with OMI averaging kernels.

Fig. 9. Tropospheric O_3 columns in 2015-2020 (annual and seasonal averages) from (A1-A5) GEOS-Chem a priori simulation (Exp. #1); (B1-B5) Assimilations of MEE surface O_3 observations (Exp. #5); (C1-C5) Assimilations of OMI O_3 observations (Exp. #8). (D1-D5) Difference in tropospheric O_3 columns calculated by OMI-based assimilations minus MEE-based assimilations (Exp. #8 minus #5). (E1-E5) Effects of seasonal variabilities in background O_3 (Exp. #3 minus #1); (F1-F5) Effects of O_3 formation within the North China Plain PBL (Exp. #4 minus #1). The output O_3 profiles are NOT convolved with OMI averaging kernels.

Fig. 10. Trends of tropospheric O_3 columns in 2015-2020 (annual and seasonal averages) from (A1-A5) GEOS-Chem a priori simulation (Exp. #1); (B1-B5) Assimilations of MEE surface O_3 observations (Exp. #5); (C1-C5) Assimilations of OMI O_3 observations (Exp. #8). (D1-D5) Effects of interannual variabilities in background O_3 (Exp. #1 minus #2). The output O_3 profiles are NOT convolved with OMI averaging kernels.

References

Benavides, J., Guevara, M., Snyder, M. G., Rodríguez-Rey, D., Soret, A., Pérez García-Pando, C., and Jorba, O.: On the impact of excess diesel NO_x emissions upon NO_2 pollution in a compact city, Environ Res Let, 16, 10.1088/1748-9326/abd5dd, 2021.

Chang, K. L., Guillas, S., and Fioletov, V. E.: Spatial mapping of ground-based observations of total ozone, Atmos Meas Tech, 8, 4487-4505, 10.5194/amt-8-4487-2015, 2015.

Chen, J., Jiang, Z., Li, R., Liao, C., Miyazaki, K., and Jones, D. B. A.: Large discrepancy between observed and modeled wintertime tropospheric NO_2 variabilities due to COVID-19 controls in China, Environ Res Let, 17, 035007, 10.1088/1748-9326/ac4ec0, 2022.

Chen, X., Jiang, Z., Shen, Y., Li, R., Fu, Y., Liu, J., Han, H., Liao, H., Cheng, X., Jones, D. B. A., Worden, H., and Abad, G. G.: Chinese Regulations Are Working—Why Is Surface Ozone Over Industrialized Areas Still High? Applying Lessons From Northeast US Air Quality Evolution, Geophys Res Lett, 48, e2021GL092816, 10.1029/2021gl092816, 2021.

Dufour, G., Hauglustaine, D., Zhang, Y., Eremenko, M., Cohen, Y., Gaudel, A., Siour, G., Lachatre, M., Bense, A., Bessagnet, B., Cuesta, J., Ziemke, J., Thouret, V., and Zheng, B.: Recent ozone trends in the Chinese free troposphere: role of the local emission reductions and meteorology, Atmos Chem Phys, 21, 16001-16025, 10.5194/acp-21-16001-2021, 2021.

Elguindi, N., Granier, C., Stavrakou, T., Darras, S., Bauwens, M., Cao, H., Chen, C., Denier van der Gon, H. A. C., Dubovik, O., Fu, T. M., Henze, D. K., Jiang, Z., Keita, S., Kuenen, J. J. P., Kurokawa, J., Liousse, C., Miyazaki, K., Müller, J. F., Qu, Z., Solmon, F., and Zheng, B.: Intercomparison of Magnitudes and Trends in Anthropogenic Surface Emissions From Bottom‐Up Inventories, Top‐Down Estimates, and Emission Scenarios, Earth's Future, 8, e2020EF001520, 10.1029/2020ef001520, 2020.

Fu, D., Kulawik, S. S., Miyazaki, K., Bowman, K. W., Worden, J. R., Eldering, A., Livesey, N. J., Teixeira, J., Irion, F. W., Herman, R. L., Osterman, G. B., Liu, X., Levelt, P. F., Thompson, A. M., and Luo, M.: Retrievals of tropospheric ozone profiles from the synergism of AIRS and OMI: methodology and validation, Atmos Meas Tech, 11, 5587-5605, 10.5194/amt-11-5587-2018, 2018.

Han, H., Liu, J., Yuan, H., Zhuang, B., Zhu, Y., Wu, Y., Yan, Y., and Ding, A.: Characteristics of intercontinental transport of tropospheric ozone from Africa to Asia, Atmos Chem Phys, 18, 4251-4276, 10.5194/acp-18-4251-2018, 2018.

Han, W., He, T.-L., Tang, Z., Wang, M., Jones, D., and Jiang, Z.: A comparative analysis for a deep learning model (hyDL-CO v1.0) and Kalman filter to predict CO concentrations in China, Geosci Model Dev, 15, 4225-4237, 10.5194/gmd-15-4225-2022, 2022.

Hoesly, R. M., Smith, S. J., Feng, L., Klimont, Z., Janssens-Maenhout, G., Pitkanen, T., Seibert, J. J., Vu, L., Andres, R. J., Bolt, R. M., Bond, T. C., Dawidowski, L., Kholod, N., Kurokawa, J.-i., Li, M., Liu, L., Lu, Z., Moura, M. C. P., O'Rourke, P. R., and Zhang, Q.: Historical (1750–2014) anthropogenic emissions of reactive gases and aerosols from the Community Emissions Data System (CEDS), Geosci Model Dev, 11, 369-408, 10.5194/gmd-11-369-2018, 2018.

Huang, G., Liu, X., Chance, K., Yang, K., Bhartia, P. K., Cai, Z., Allaart, M., Ancellet, G., Calpini, B., Coetzee, G. J. R., Cuevas-Agulló, E., Cupeiro, M., De Backer, H., Dubey, M. K., Fuelberg, H. E., Fujiwara, M., Godin-Beekmann, S., Hall, T. J., Johnson, B., Joseph, E., Kivi, R., Kois, B., Komala, N., König-Langlo, G., Laneve, G., Leblanc, T., Marchand, M., Minschwaner, K. R., Morris, G., Newchurch, M. J., Ogino, S.-Y., Ohkawara, N., Piters, A. J. M., Posny, F., Querel, R., Scheele, R., Schmidlin, F. J., Schnell, R. C., Schrems, O., Selkirk, H., Shiotani, M., Skrivánková, P., Stübi, R., Taha, G., Tarasick, D. W., Thompson, A. M., Thouret, V., Tully, M. B., Van Malderen, R., Vömel, H., von der Gathen, P., Witte, J. C., and Yela, M.: Validation of 10-year SAO OMI Ozone Profile (PROFOZ) product using ozonesonde observations, Atmos Meas Tech, 10, 2455-2475, 10.5194/amt-10-2455-2017, 2017.

Huijnen, V., Miyazaki, K., Flemming, J., Inness, A., Sekiya, T., and Schultz, M. G.: An intercomparison of tropospheric ozone reanalysis products from CAMS, CAMS interim, TCR-1, and TCR-2, Geosci Model Dev, 13, 1513-1544, 10.5194/gmd-13-1513-2020, 2020.

Iglesias-Suarez, F., Kinnison, D. E., Rap, A., Maycock, A. C., Wild, O., and Young, P. J.: Key drivers of ozone change and its radiative forcing over the 21st century, Atmos Chem Phys, 18, 6121-6139, 10.5194/acp-18-6121-2018, 2018.

Jiang, Z., Miyazaki, K., Worden, J. R., Liu, J. J., Jones, D. B. A., and Henze, D. K.: Impacts of anthropogenic and natural sources on free tropospheric ozone over the Middle East, Atmos Chem Phys, 16, 6537-6546, 10.5194/acp-16-6537-2016, 2016.

Jiang, Z., Zhu, R., Miyazaki, K., McDonald, B. C., Klimont, Z., Zheng, B., Boersma, K. F., Zhang, Q., Worden, H., Worden, J. R., Henze, D. K., Jones, D. B. A., Denier van der Gon, H. A. C., and Eskes, H.: Decadal Variabilities in Tropospheric Nitrogen Oxides Over United States, Europe, and China, J Geophys Res-Atmos, 127, e2021JD035872, 10.1029/2021jd035872, 2022.

Li, D., Shindell, D., Ding, D., Lu, X., Zhang, L., and Zhang, Y.: Surface ozone impacts on major crop production in China from 2010 to 2017, Atmos Chem Phys, 22, 2625-2638, 10.5194/acp-22-2625-2022, 2022.

Li, K., Jacob, D. J., Liao, H., Shen, L., Zhang, Q., and Bates, K. H.: Anthropogenic drivers of 2013-2017 trends in summer surface ozone in China, Proc Natl Acad Sci USA, 116, 422-427, 10.1073/pnas.1812168116, 2019.

Li, M., Zhang, Q., Kurokawa, J.-i., Woo, J.-H., He, K., Lu, Z., Ohara, T., Song, Y., Streets, D. G., Carmichael, G. R., Cheng, Y., Hong, C., Huo, H., Jiang, X., Kang, S., Liu, F., Su, H., and

Zheng, B.: MIX: a mosaic Asian anthropogenic emission inventory under the international collaboration framework of the MICS-Asia and HTAP, Atmos Chem Phys, 17, 935-963, 10.5194/acp-17-935-2017, 2017.
Li, M., Zhang, Q., Zheng, B., Tong, D., Lei, Y., Liu, F., Hong, C., Kang, S., Yan, L., Zhang, Y., Bo, Y., Su, H., Cheng, Y., and He, K.: Persistent growth of anthropogenic non-methane volatile organic compound (NMVOC) emissions in China during 1990–2017: drivers, speciation and ozone formation potential, Atmos Chem Phys, 19, 8897-8913, 10.5194/acp-19-8897-2019, 2019.
Li, R., Zhao, Y., Zhou, W., Meng, Y., Zhang, Z., and Fu, H.: Developing a novel hybrid model for the estimation of surface 8 h ozone (O_3) across the remote Tibetan Plateau during 2005–2018, Atmos Chem Phys, 20, 6159-6175, 10.5194/acp-20-6159-2020, 2020.
Liu, X., Bhartia, P. K., Chance, K., Spurr, R. J. D., and Kurosu, T. P.: Ozone profile retrievals from the Ozone Monitoring Instrument, Atmos Chem Phys, 10, 2521-2537, 10.5194/acp-10-2521-2010, 2010.
Liu, X., Zhu, Y., Xue, L., Desai, A. R., and Wang, H.: Cluster‐Enhanced Ensemble Learning for Mapping Global Monthly Surface Ozone From 2003 to 2019, Geophys Res Lett, 49, e2022GL097947, 10.1029/2022gl097947, 2022.
Liu, Z., Doherty, R. M., Wild, O., Hollaway, M., and O'Connor, F. M.: Contrasting chemical environments in summertime for atmospheric ozone across major Chinese industrial regions: the effectiveness of emission control strategies, Atmos Chem Phys, 21, 10689-10706, 10.5194/acp-21-10689-2021, 2021.
Logan, J. A., Staehelin, J., Megretskaia, I. A., Cammas, J. P., Thouret, V., Claude, H., De Backer, H., Steinbacher, M., Scheel, H. E., Stübi, R., Fröhlich, M., and Derwent, R.: Changes in ozone over Europe: Analysis of ozone measurements from sondes, regular aircraft (MOZAIC) and alpine surface sites, J Geophys Res-Atmos, 117, n/a-n/a, 10.1029/2011jd016952, 2012.
Ma, C., Wang, T., Mizzi, A. P., Anderson, J. L., Zhuang, B., Xie, M., and Wu, R.: Multiconstituent Data Assimilation With WRF‐Chem/DART: Potential for Adjusting Anthropogenic Emissions and Improving Air Quality Forecasts Over Eastern China, J Geophys Res-Atmos, 7393–7412, 10.1029/2019jd030421, 2019.
Mickley, L. J.: Climate response to the increase in tropospheric ozone since preindustrial times: A comparison between ozone and equivalent CO2forcings, Journal of Geophysical Research, 109, 10.1029/2003jd003653, 2004.
Miyazaki, K., Eskes, H., Sudo, K., Boersma, K. F., Bowman, K., and Kanaya, Y.: Decadal changes in global surface NO_x emissions from multi-constituent satellite data assimilation, Atmos Chem Phys, 17, 807-837, 10.5194/acp-17-807-2017, 2017.
Mousavinezhad, S., Choi, Y., Pouyaei, A., Ghahremanloo, M., and Nelson, D. L.: A comprehensive investigation of surface ozone pollution in China, 2015–2019: Separating the contributions from meteorology and precursor emissions, Atmospheric Research, 257, 10.1016/j.atmosres.2021.105599, 2021.

719 Oetjen, H., Payne, V. H., Neu, J. L., Kulawik, S. S., Edwards, D. P., Eldering, A., Worden, H.
720 M., and Worden, J. R.: A joint data record of tropospheric ozone from Aura-TES and MetOp-
721 IASI, Atmos Chem Phys, 16, 10229-10239, 10.5194/acp-16-10229-2016, 2016.
722 Parrington, M., Jones, D. B. A., Bowman, K. W., Horowitz, L. W., Thompson, A. M., Tarasick,
723 D. W., and Witte, J. C.: Estimating the summertime tropospheric ozone distribution over
724 North America through assimilation of observations from the Tropospheric Emission
725 Spectrometer, Journal of Geophysical Research, 113, 10.1029/2007jd009341, 2008.
726 Parrington, M., Palmer, P. I., Henze, D. K., Tarasick, D. W., Hyer, E. J., Owen, R. C., Helmig,
727 D., Clerbaux, C., Bowman, K. W., Deeter, M. N., Barratt, E. M., Coheur, P. F., Hurtmans,
728 D., Jiang, Z., George, M., and Worden, J. R.: The influence of boreal biomass burning
729 emissions on the distribution of tropospheric ozone over North America and the North
730 Atlantic during 2010, Atmos Chem Phys, 12, 2077-2098, 10.5194/acp-12-2077-2012, 2012.
731 Parrish, D. D., Derwent, R. G., Turnock, S. T., O'Connor, F. M., Staehelin, J., Bauer, S. E.,
732 Deushi, M., Oshima, N., Tsigaridis, K., Wu, T., and Zhang, J.: Investigations on the
733 anthropogenic reversal of the natural ozone gradient between northern and southern
734 midlatitudes, Atmos Chem Phys, 21, 9669-9679, 10.5194/acp-21-9669-2021, 2021.
735 Peng, X., Shen, H., Zhang, L., Zeng, C., Yang, G., and He, Z.: Spatially continuous mapping
736 of daily global ozone distribution (2004–2014) with the Aura OMI sensor, J Geophys Res-
737 Atmos, 121, 12,702-712,722, 10.1002/2016jd025013, 2016.
738 Peng, X., Wang, W., Xia, M., Chen, H., Ravishankara, A. R., Li, Q., Saiz-Lopez, A., Liu, P.,
739 Zhang, F., Zhang, C., Xue, L., Wang, X., George, C., Wang, J., Mu, Y., Chen, J., and Wang,
740 T.: An unexpected large continental source of reactive bromine and chlorine with significant
741 impact on wintertime air quality, Natl Sci Rev, 8, nwaa304, 10.1093/nsr/nwaa304, 2021.
742 Prinn, R. G.: The Cleansing Capacity of the Atmosphere, Annual Review of Environment and
743 Resources, 28, 29-57, 10.1146/annurev.energy.28.011503.163425, 2003.
744 Schaap, M., Cuvelier, C., Hendriks, C., Bessagnet, B., Baldasano, J. M., Colette, A., Thunis,
745 P., Karam, D., Fagerli, H., Graff, A., Kranenburg, R., Nyiri, A., Pay, M. T., Rouïl, L., Schulz,
746 M., Simpson, D., Stern, R., Terrenoire, E., and Wind, P.: Performance of European chemistry
747 transport models as function of horizontal resolution, Atmos Environ, 112, 90-105,
748 10.1016/j.atmosenv.2015.04.003, 2015.
749 Spurr, R. J. D.: VLIDORT: A linearized pseudo-spherical vector discrete ordinate radiative
750 transfer code for forward model and retrieval studies in multilayer multiple scattering media,
751 Journal of Quantitative Spectroscopy and Radiative Transfer, 102, 316-342,
752 10.1016/j.jqsrt.2006.05.005, 2006.
753 Tang, Z., Chen, J., and Jiang, Z.: Discrepancy in assimilated atmospheric CO over East Asia
754 in 2015–2020 by assimilating satellite and surface CO measurements, Atmos Chem Phys, 22,
755 7815-7826, 10.5194/acp-22-7815-2022, 2022.
756 Thompson, A. M.: The oxidizing capacity of the earth's atmosphere: probable past and future
757 changes, Science, 256, 1157-1165, 10.1126/science.256.5060.1157, 1992.
758 van der Werf, G. R., Randerson, J. T., Giglio, L., Collatz, G. J., Mu, M., Kasibhatla, P. S.,
759 Morton, D. C., DeFries, R. S., Jin, Y., and van Leeuwen, T. T.: Global fire emissions and the

contribution of deforestation, savanna, forest, agricultural, and peat fires (1997–2009), Atmos Chem Phys, 10, 11707-11735, 10.5194/acp-10-11707-2010, 2010.
Wang, W., Parrish, D. D., Wang, S., Bao, F., Ni, R., Li, X., Yang, S., Wang, H., Cheng, Y., and Su, H.: Long-term trend of ozone pollution in China during 2014–2020: distinct seasonal and spatial characteristics and ozone sensitivity, Atmos Chem Phys, 22, 8935-8949, 10.5194/acp-22-8935-2022, 2022.
Wang, X., Fu, T. M., Zhang, L., Lu, X., Liu, X., Amnuaylojaroen, T., Latif, M. T., Ma, Y., Zhang, L., Feng, X., Zhu, L., Shen, H., and Yang, X.: Rapidly Changing Emissions Drove Substantial Surface and Tropospheric Ozone Increases Over Southeast Asia, Geophys Res Lett, 49, e2022GL100223, 10.1029/2022gl100223, 2022.
Wei, J., Li, Z., Li, K., Dickerson, R. R., Pinker, R. T., Wang, J., Liu, X., Sun, L., Xue, W., and Cribb, M.: Full-coverage mapping and spatiotemporal variations of ground-level ozone (O_3) pollution from 2013 to 2020 across China, Remote Sens Environ, 270, 10.1016/j.rse.2021.112775, 2022.
Zhang, L., Jacob, D. J., Boersma, K. F., Jaffe, D. A., Olson, J. R., Bowman, K. W., Worden, J. R., Thompson, A. M., Avery, M. A., Cohen, R. C., Dibb, J. E., Flock, F. M., Fuelberg, H. E., Huey, L. G., McMillan, W. W., Singh, H. B., and Weinheimer, A. J.: Transpacific transport of ozone pollution and the effect of recent Asian emission increases on air quality in North America: an integrated analysis using satellite, aircraft, ozonesonde, and surface observations, Atmos Chem Phys, 8, 6117-6136, DOI 10.5194/acp-8-6117-2008, 2008.
Zhang, Y., Shindell, D., Seltzer, K., Shen, L., Lamarque, J.-F., Zhang, Q., Zheng, B., Xing, J., Jiang, Z., and Zhang, L.: Impacts of emission changes in China from 2010 to 2017 on domestic and intercontinental air quality and health effect, Atmos Chem Phys, 21, 16051-16065, 10.5194/acp-21-16051-2021, 2021.
Zheng, B., Tong, D., Li, M., Liu, F., Hong, C., Geng, G., Li, H., Li, X., Peng, L., Qi, J., Yan, L., Zhang, Y., Zhao, H., Zheng, Y., He, K., and Zhang, Q.: Trends in China's anthropogenic emissions since 2010 as the consequence of clean air actions, Atmos Chem Phys, 18, 14095-14111, 10.5194/acp-18-14095-2018, 2018.
Zhu, R., Tang, Z., Chen, X., Liu, X., and Jiang, Z.: Rapid O_3 assimilations – Part 2: tropospheric O_3 changes accompanied by declines in NO_x emissions in the United States and Europe in 2005-2020, Atmos. Chem. Phys. Discuss., 10.5194/acp-2023-47, 2023.
Zhu, Y., Liu, J., Wang, T., Zhuang, B., Han, H., Wang, H., Chang, Y., and Ding, K.: The Impacts of Meteorology on the Seasonal and Interannual Variabilities of Ozone Transport From North America to East Asia, J Geophys Res-Atmos, 122, 10,612-610,636, 10.1002/2017jd026761, 2017.
Ziemke, J. R., Oman, L. D., Strode, S. A., Douglass, A. R., Olsen, M. A., McPeters, R. D., Bhartia, P. K., Froidevaux, L., Labow, G. J., Witte, J. C., Thompson, A. M., Haffner, D. P., Kramarova, N. A., Frith, S. M., Huang, L.-K., Jaross, G. R., Seftor, C. J., Deland, M. T., and Taylor, S. L.: Trends in global tropospheric ozone inferred from a composite record of TOMS/OMI/MLS/OMPS satellite measurements and the MERRA-2 GMI simulation, Atmos Chem Phys, 19, 3257-3269, 10.5194/acp-19-3257-2019, 2019.

	Experiments	Observations	O3 Boundary Conditions	Other Settings
A priori Simulations	#1 (Main)	N/A	Original (2015-2020)	
	#2	N/A	Original (2015, fixed)	
	#3	N/A	Original (2015-2020, fixed in spring)	
	#4	N/A	Original (2015-2020)	PO3 = 0 (NCP)
Kalman Filter Assimilations	#5 (Main)	MEE	Original (2015-2020)	γ = 0.8
	#6	MEE	Original (2015-2020)	γ = 0.0
	#7	MEE	Original (2015-2020)	γ = 1.0
	#8 (Main)	OMI	Optimized (2015-2020)	positions: 4-11
	#9	OMI	Original (2015-2020)	positions: 4-11
	#10	OMI	Optimized (2015-2020)	positions: 4-27

Table. 1. Single O_3 tracer simulation and assimilation experiments (Exp.) conducted in this work. Exp. #1: the main a priori simulation; Exp. #2: O_3 boundary conditions and stratospheric O_3 concentrations are fixed in 2015; Exp. #3: O_3 boundary conditions and stratospheric O_3 concentrations are fixed in the spring; Exp. #4: O_3 formation rates within the North China Plain PBL are set to zero; Exp. #5: the main assimilation by assimilating MEE surface O_3 observations with $\gamma = 0.8$; Exp. #6: only surface O_3 concentrations are adjusted ($\gamma = 0$); Exp. #7: full mixing of O_3 biases within the PBL ($\gamma = 1.0$); Exp. #8: the main assimilation by assimilating OMI O_3 observations; Exp. #9: O_3 boundary conditions are not optimized; Exp. #10: assimilating OMI O_3 observations at across-track positions 4-27.

E. China (2015-2020)		Annual		Spring		Summer		Autumn		Winter	
		Mean	Trend	Mean	Trend	Mean	Trend	Mean	Trend	Mean	Trend
T2.1 surface (sampled)	MEE	42.1±0.3	1.77±0.38	48.4±0.4	2.25±0.46	51.7±0.6	1.70±0.64	39.8±0.4	2.01±0.60	29.6±0.2	1.14±0.49
	a priori	43.2±0.2	0.21±0.13	48.0±0.2	0.31±0.15	56.3±0.5	-0.12±0.38	40.1±0.3	0.45±0.19	28.5±0.3	0.40±0.17
	KF-MEE	41.8±0.2	1.24±0.28	47.2±0.3	1.60±0.34	51.7±0.5	1.16±0.55	39.5±0.3	1.47±0.47	29.5±0.2	0.80±0.37
T2.2 surface	a priori	42.6±0.1	0.10±0.11	47.7±0.1	0.16±0.11	53.1±0.2	-0.19±0.29	39.1±0.1	0.25±0.19	30.8±0.2	0.35±0.13
	KF-MEE	41.3±0.1	0.55±0.17	46.7±0.1	0.71±0.17	49.8±0.2	0.36±0.36	38.0±0.1	0.69±0.31	31.0±0.2	0.54±0.19
T2.3 trop. column (convolved)	OMI	38.0±0.2	-0.30±0.19	40.9±0.2	0.12±0.20	45.9±0.2	-0.66±0.44	34.6±0.2	-0.41±0.30	30.4±0.2	-0.48±0.40
	a priori	37.1±0.1	0.02±0.14	41.0±0.2	0.17±0.24	43.2±0.2	-0.19±0.16	32.6±0.1	0.15±0.19	31.3±0.2	-0.06±0.18
	KF-OMI	37.9±0.1	-0.17±0.15	41.1±0.2	0.08±0.07	45.5±0.2	-0.51±0.37	34.2±0.1	-0.17±0.24	30.7±0.1	-0.17±0.23
T2.4 trop. Column	a priori	38.3±0.1	0.07±0.14	42.8±0.2	-0.02±0.46	42.5±0.2	0.02±0.16	33.3±0.1	0.29±0.11	34.8±0.2	0.09±0.32
	KF-MEE	37.9±0.1	0.17±0.16	42.6±0.2	0.09±0.47	41.8±0.2	0.17±0.15	33.0±0.1	0.38±0.12	34.7±0.2	0.12±0.32
	KF-OMI	38.8±0.1	-0.10±0.25	42.9±0.2	-0.17±0.57	44.1±0.2	-0.22±0.26	34.4±0.1	0.04±0.12	34.2±0.2	-0.02±0.30

Table. 2. Averages (with units ppb or DU) and trends (with units ppb yr^{-1} or DU yr^{-1}) of surface and tropospheric column O_3 concentrations in 2015-2020 over E. China from observations (MEE and OMI) and a priori (Exp. #1) and a posteriori (KF) simulations (Exp. #5 and #8). T2.1): the modeled surface O_3 is sampled at the locations and times of MEE surface O_3 observations; T2.2): the modeled surface O_3 is averaged over E. China (land only); T2.3): the output O_3 profiles from the a priori and a posteriori simulations are convolved with OMI O_3 averaging kernels; T2.4): the output O_3 profiles are NOT convolved with OMI O_3 averaging kernels. The uncertainties in the averages are calculated using the bootstrapping method. The trends and uncertainties in the trends are calculated using the linear fitting of averages by using the least squares method (see details in the SI).

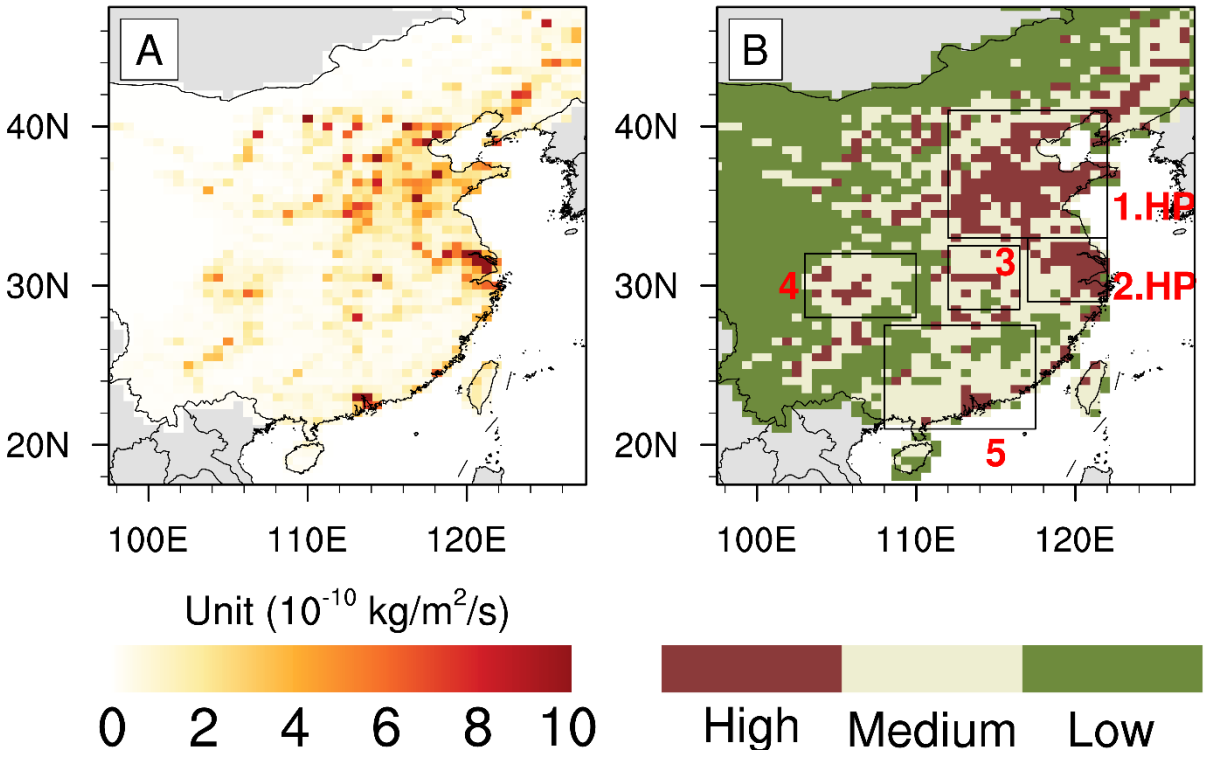

Fig. 1. (A) Anthropogenic NO_x emissions over E. China in 2015; (B) Region definitions for the North China Plain (#1), Yangtze River Delta (#2), Central China (#3), Sichuan Basin (#4) and Southern China (#5). The different colors (red, gray and green) represent grids with high (highest 15%), medium (15-50%) and low (lowest 50%) anthropogenic NO_x emissions. Regions #1 and #2 are defined as highly polluted (HP) regions by excluding grids with low and medium anthropogenic NO_x emissions.

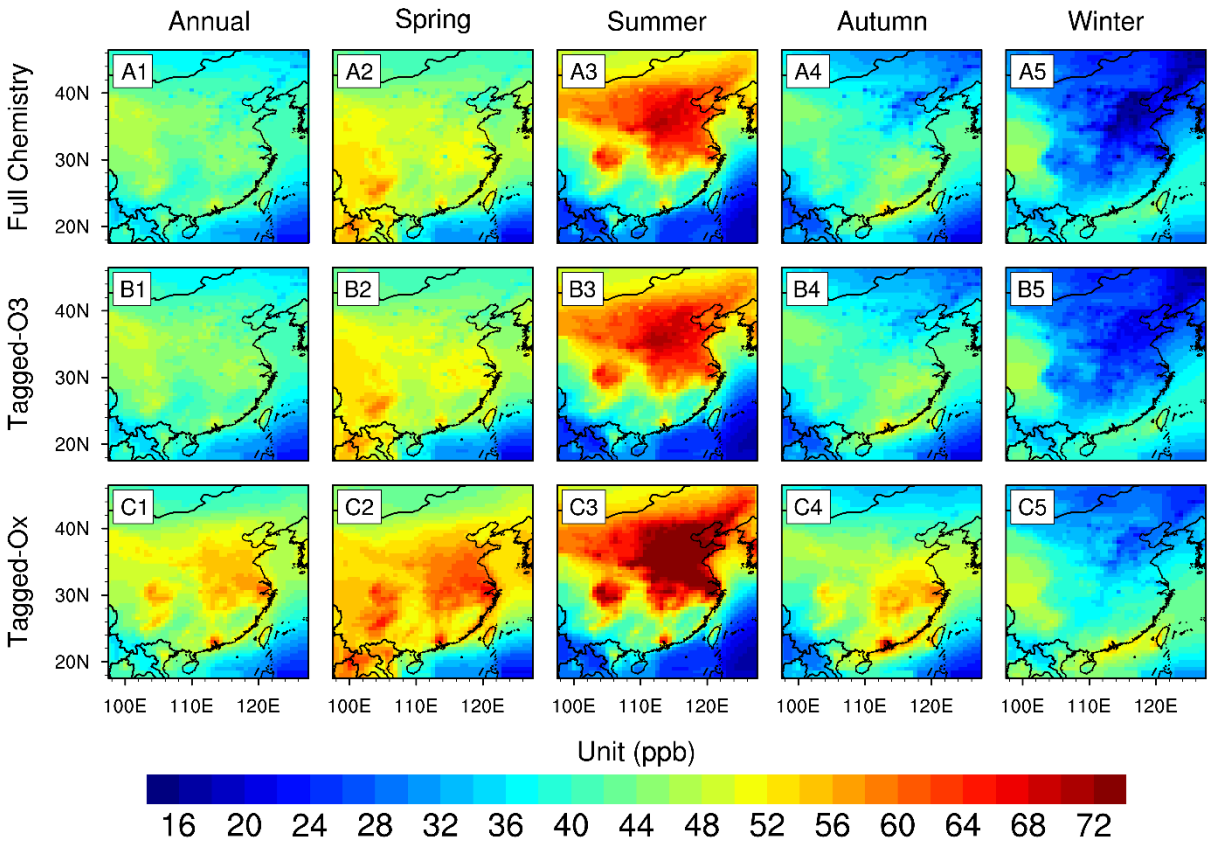

Fig. 2. Surface MDA8 O_3 in 2015-2020 (annual and seasonal averages) simulated by GEOS-Chem model with (A1-A5) full chemistry mode; (B1-B5) single O_3 tracer (tagged-O_3) mode; and (C1-C5) tagged-O_x mode. The 8-hour range of surface O_x is selected according to the time range of MDA8 O_3.

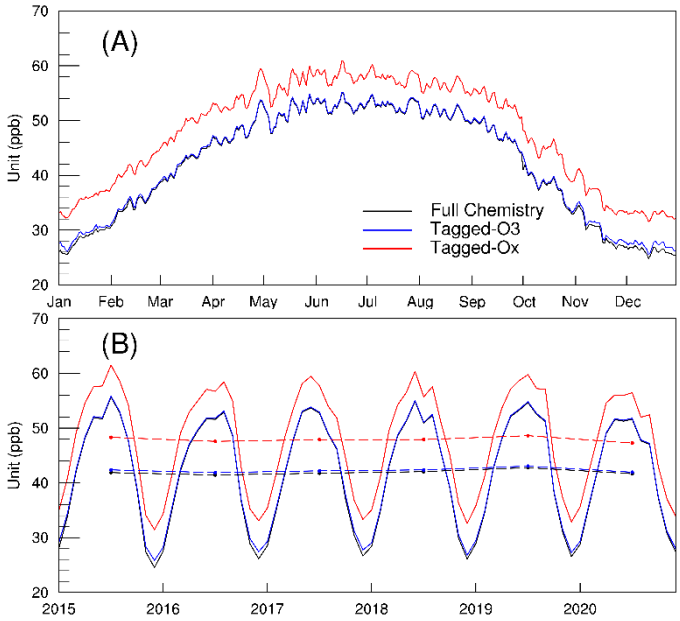

Fig. 3. (A) Daily averages of surface MDA8 O_3 over E. China in 2015-2020 from GEOS-Chem full chemistry (black), single O_3 tracer (tagged-O_3) (blue) and tagged-O_x (red) simulations; (B) Monthly averages of MDA8 O_3. The dashed lines in panel B are annual averages.

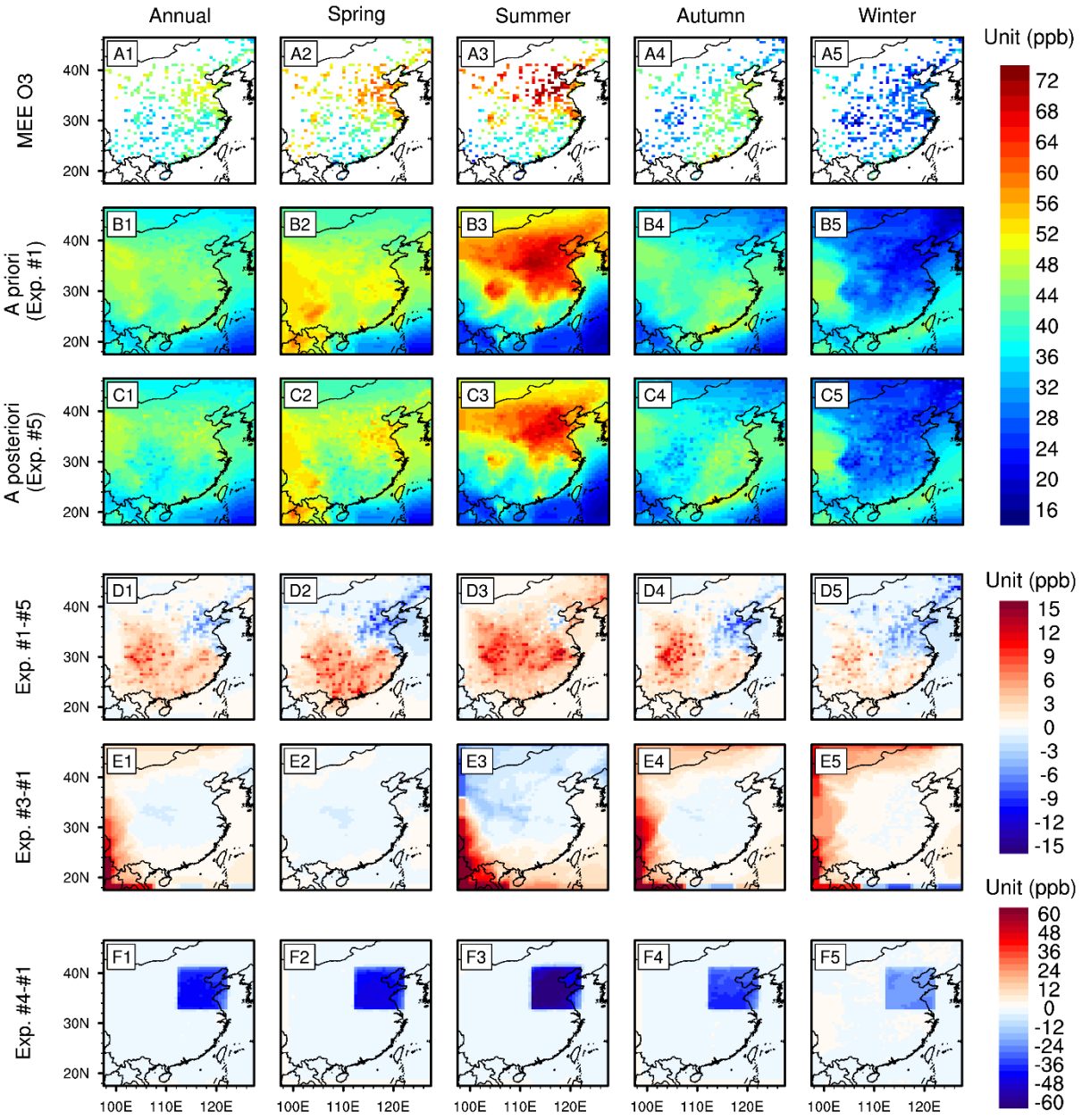

Fig. 4. Surface MDA8 O_3 in 2015-2020 (annual and seasonal averages) from (A1-A5) MEE stations; (B1-B5) GEOS-Chem a priori simulation (Exp. #1); (C1-C5) GEOS-Chem a posteriori simulation by assimilating MEE O_3 observations (Exp. #5); (D1-D5) Bias in the a priori simulations (Exp. #1 minus #5). (E1-E5) Effects of seasonal variabilities in background O_3 (Exp. #3 minus #1); (F1-F5) Effects of O_3 formation within the North China Plain PBL (Exp. #4 minus #1).

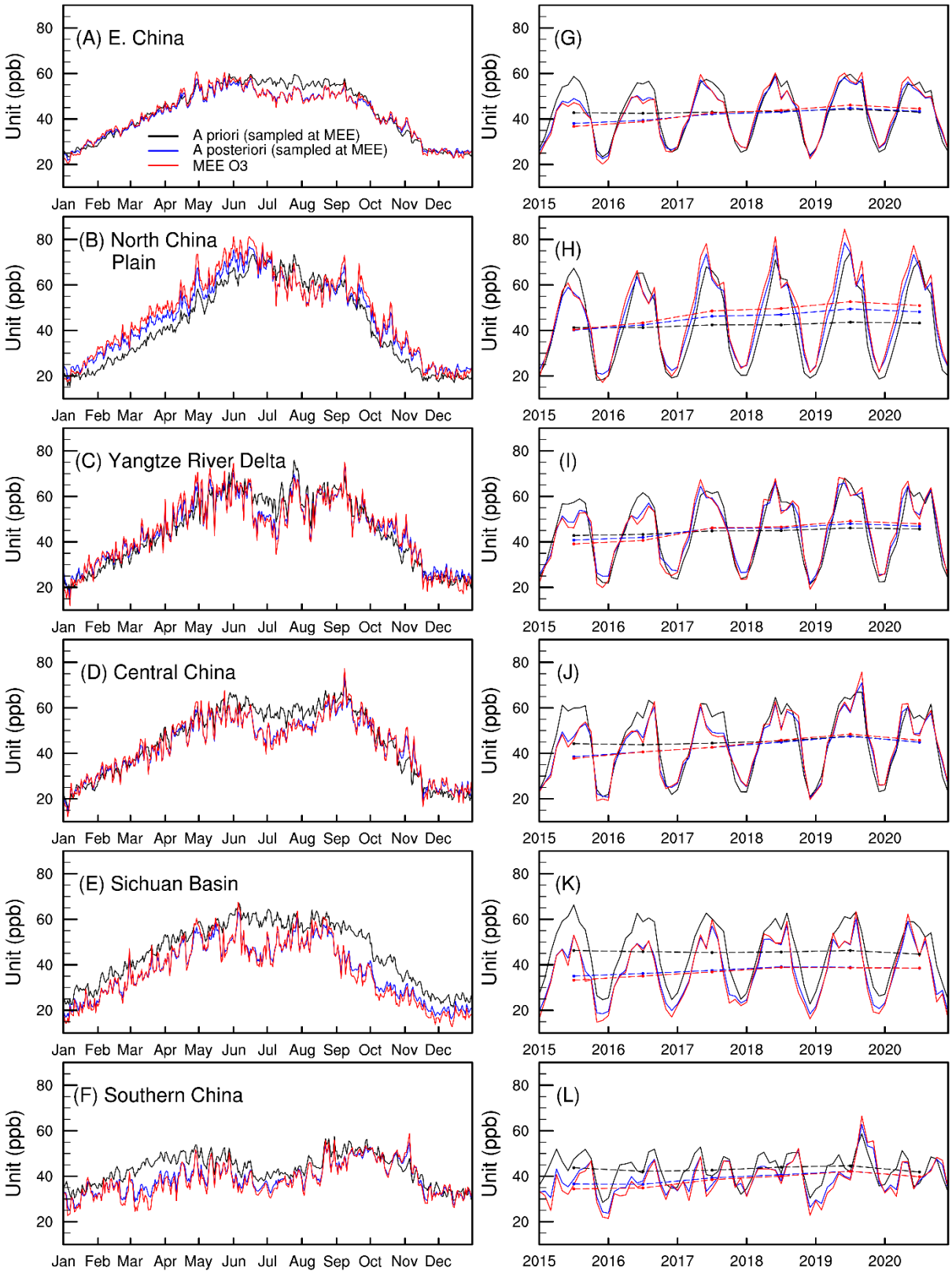

Fig. 5. (A-F) Daily averages of surface MDA8 O_3 in 2015-2020 from MEE stations (red) and GEOS-Chem a priori (black, Exp. #1) and a posteriori (blue, Exp. #5) simulations by assimilating MEE O_3 observations. (G-L) Monthly averages of MDA8 O_3. The dashed lines in panels G-L are annual averages.

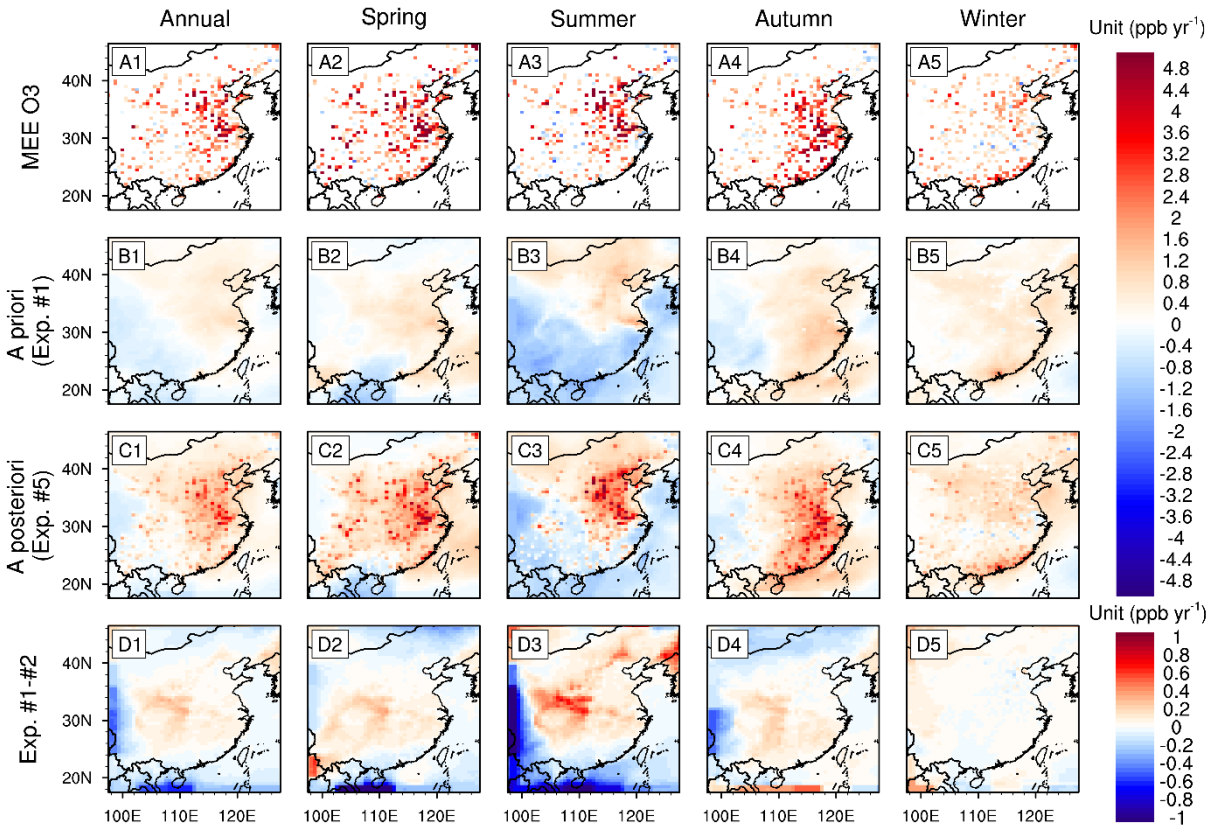

Fig. 6. Trends of surface MDA8 O_3 in 2015-2020 (annual and seasonal averages) from (A1-A5) MEE stations; (B1-B5) GEOS-Chem a priori simulation (Exp. #1); (C1-C5) GEOS-Chem a posteriori simulation by assimilating MEE O_3 observations (Exp. #5). (D1-D5) Effects of interannual variabilities in background O_3 (Exp. #1 minus #2).

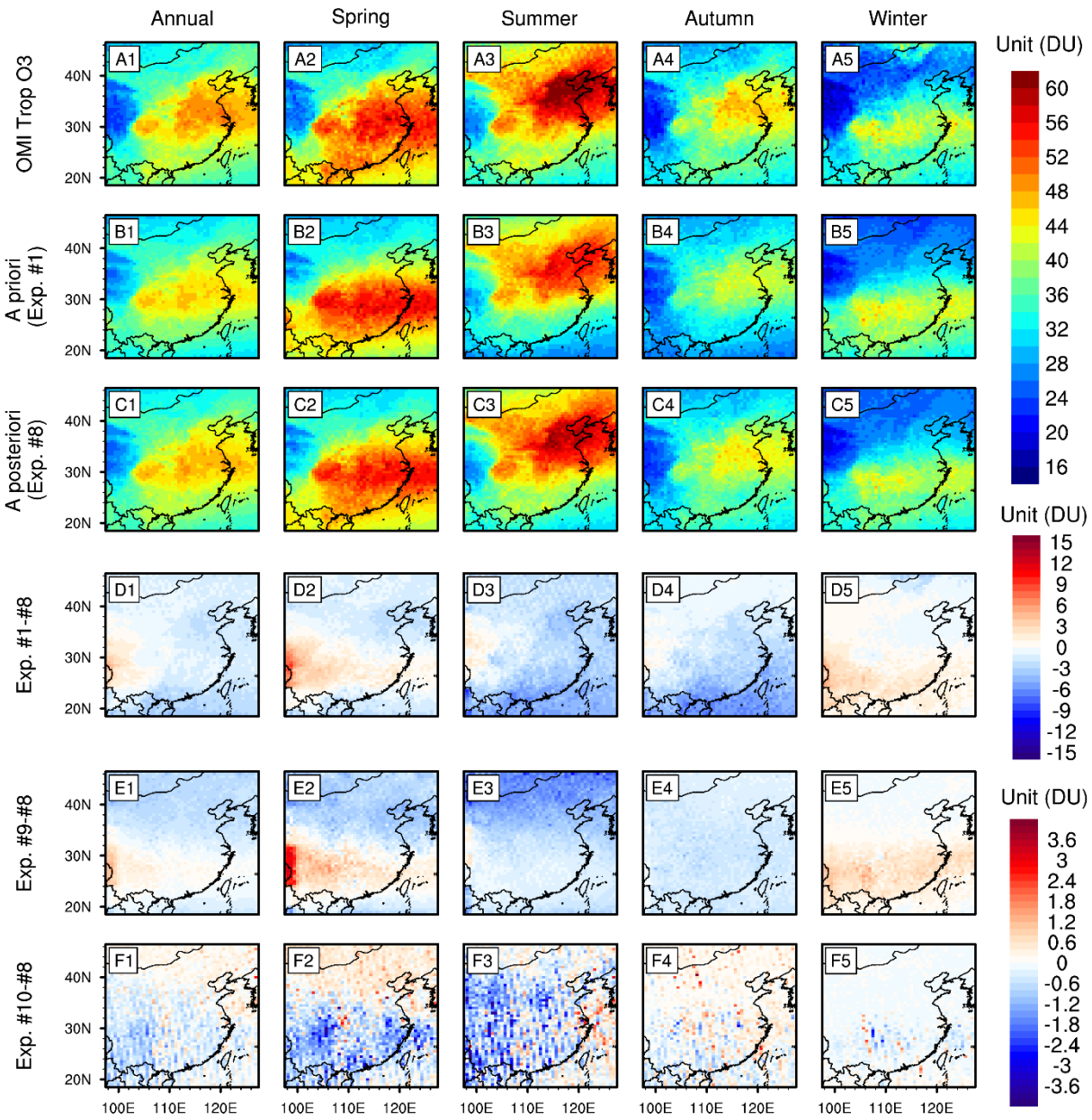

Fig. 7. Tropospheric O_3 columns in 2015-2020 (annual and seasonal averages) from (A1-A5) OMI observations; (B1-B5) GEOS-Chem a priori simulation (Exp. #1); (C1-C5) GEOS-Chem a posteriori simulation by assimilating OMI O_3 observations (Exp. #8). (D1-D5) Bias in the a priori simulations (Exp. #1 minus #8). (E1-E5) Effects of optimization on regional O_3 background conditions (Exp. #9 minus #8); (F1-F5) Effects of the usage of row-isolated data (Exp. #10 minus #8). The output O_3 profiles are convolved with OMI averaging kernels.

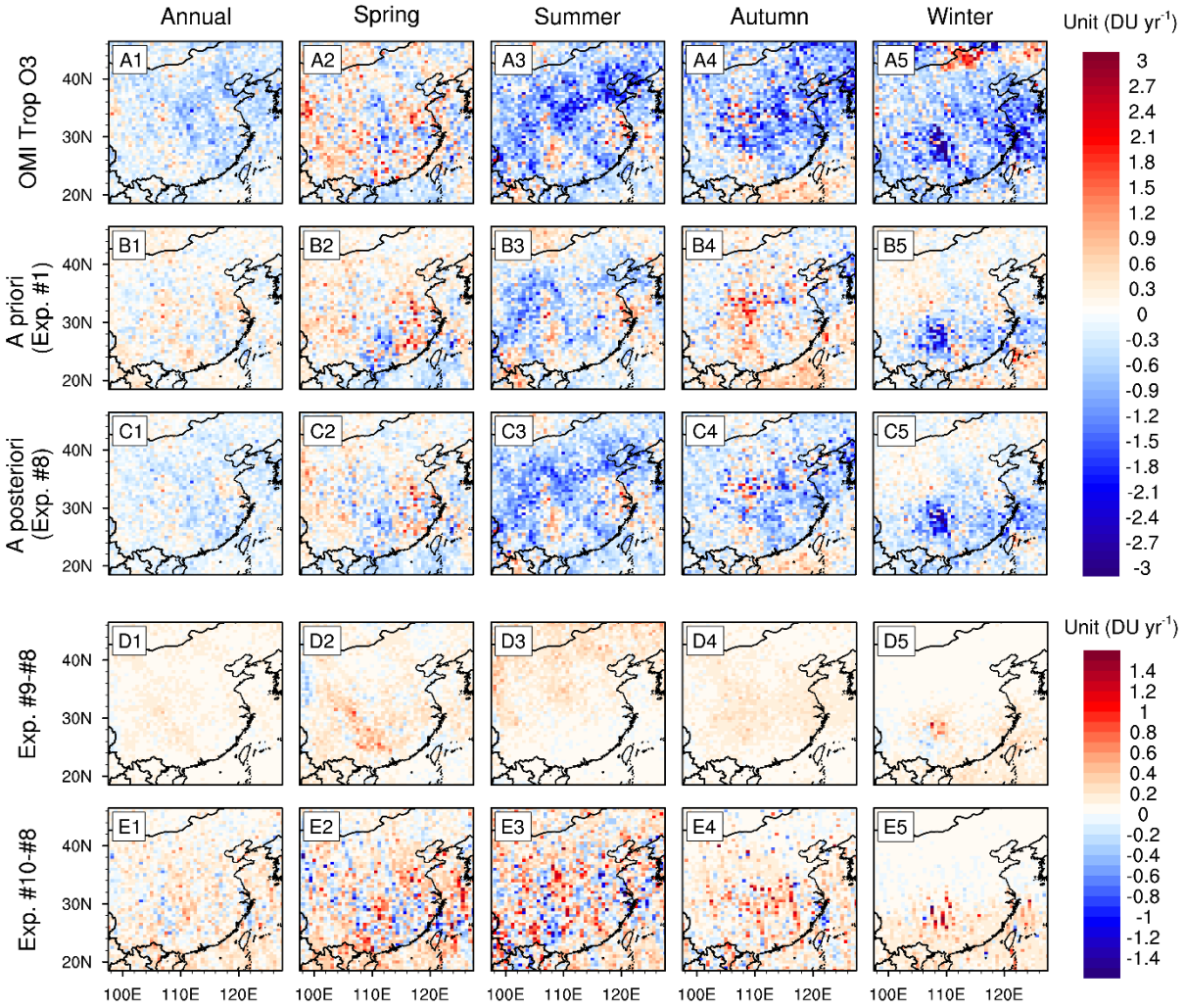

Fig. 8. Trends of tropospheric O_3 columns in 2015-2020 (annual and seasonal averages) from (A1-A5) OMI observations; (B1-B5) GEOS-Chem a priori simulation (Exp. #1); (C1-C5) GEOS-Chem a posteriori simulation by assimilating OMI O_3 observations (Exp. #8). (D1-D5) Effects of optimization on regional O_3 background conditions (Exp. #9 minus #8); (E1-E5) Effects of the usage of row-isolated data (Exp. #10 minus #8). The output O_3 profiles are convolved with OMI averaging kernels.

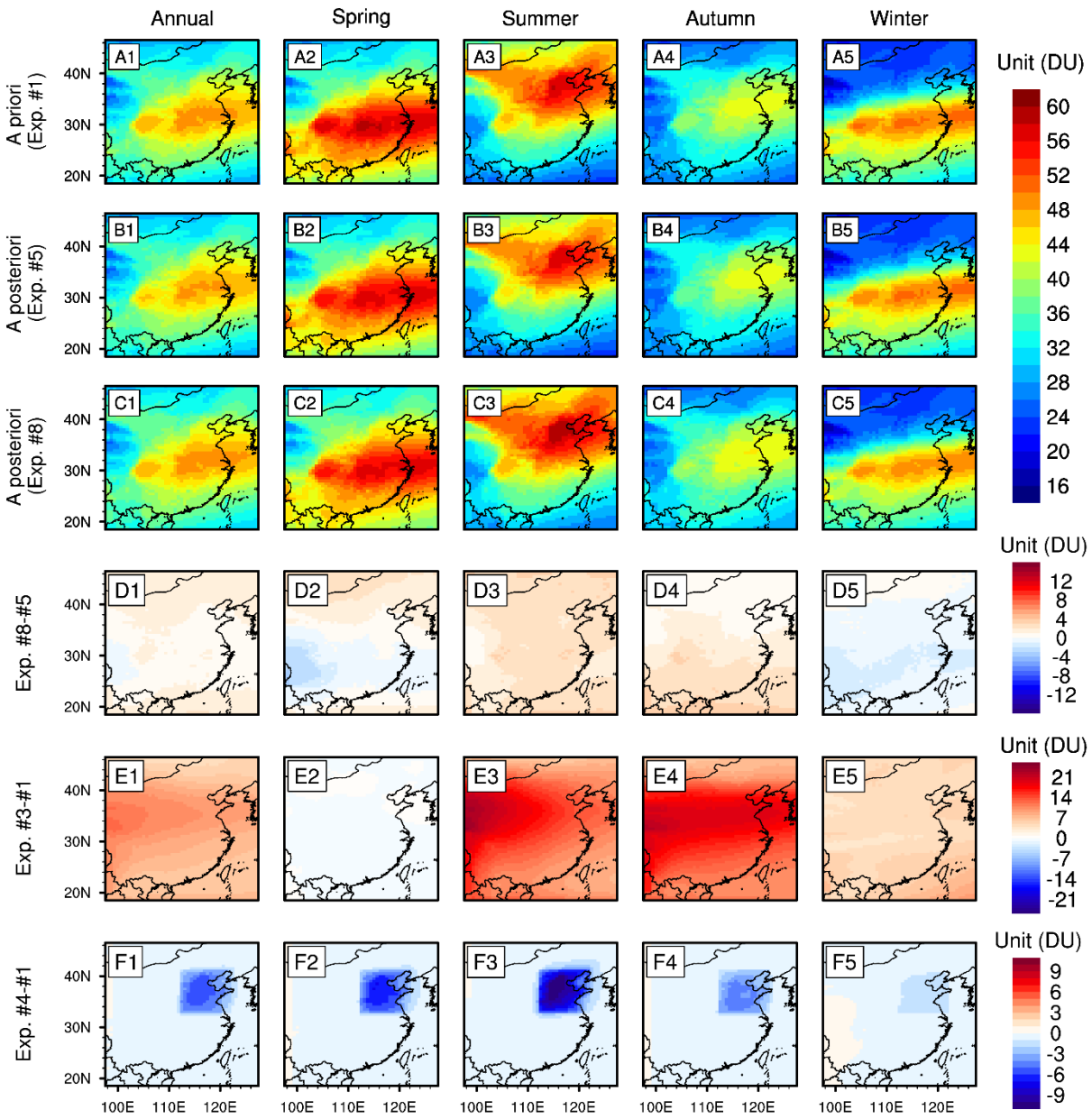

Fig. 9. Tropospheric O_3 columns in 2015-2020 (annual and seasonal averages) from (A1-A5) GEOS-Chem a priori simulation (Exp. #1); (B1-B5) Assimilations of MEE surface O_3 observations (Exp. #5); (C1-C5) Assimilations of OMI O_3 observations (Exp. #8). (D1-D5) Difference in tropospheric O_3 columns calculated by OMI-based assimilations minus MEE-based assimilations (Exp. #8 minus #5). (E1-E5) Effects of seasonal variabilities in background O_3 (Exp. #3 minus #1); (F1-F5) Effects of O_3 formation within the North China Plain PBL (Exp. #4 minus #1). The output O_3 profiles are NOT convolved with OMI averaging kernels.

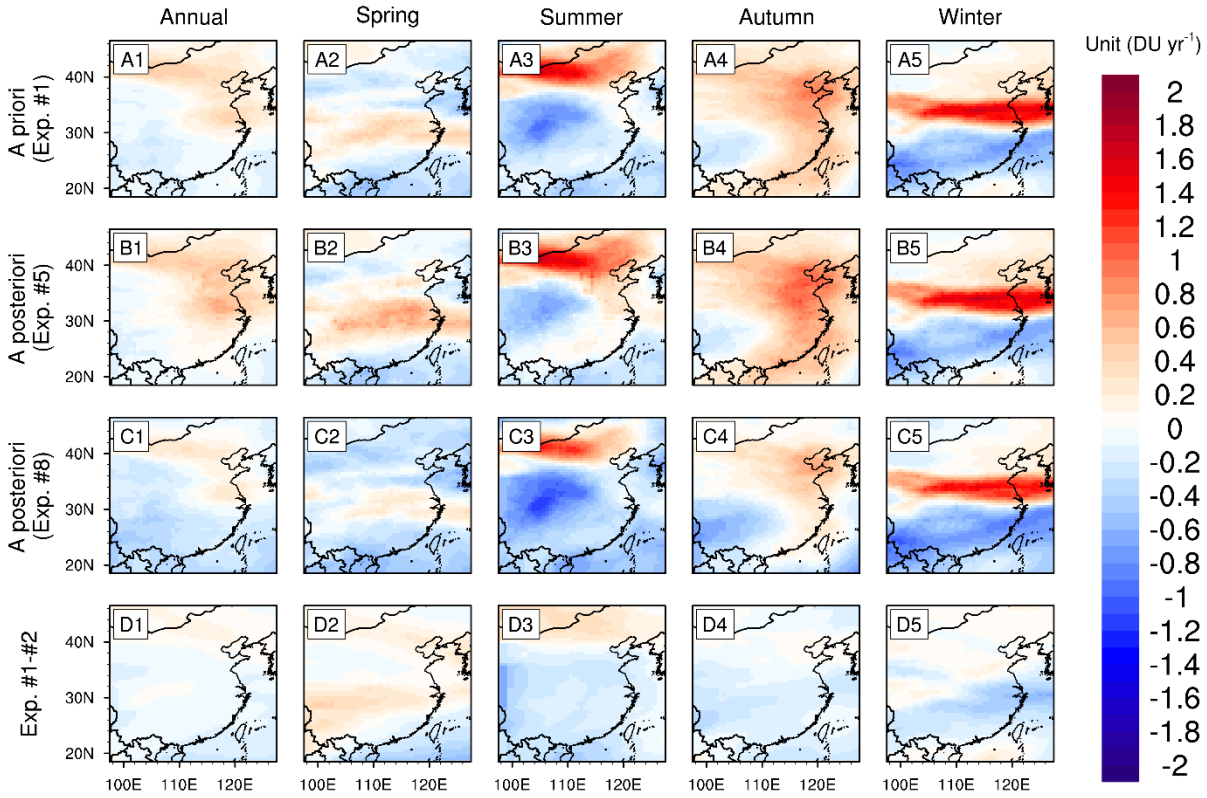

Fig. 10. Trends of tropospheric O_3 columns in 2015-2020 (annual and seasonal averages) from (A1-A5) GEOS-Chem a priori simulation (Exp. #1); (B1-B5) Assimilations of MEE surface O_3 observations (Exp. #5); (C1-C5) Assimilations of OMI O_3 observations (Exp. #8). (D1-D5) Effects of interannual variabilities in background O_3 (Exp. #1 minus #2). The output O_3 profiles are NOT convolved with OMI averaging kernels.